nature communications

Article

https://doi.org/10.1038/s41467-025-59310-3

Metabolic reprogramming driven by Ant2 deficiency augments T Cell function and anti-tumor immunity in mice

Received: 29 August 2024

Accepted: 18 April 2025

Omri Yosef[1], Leonor Cohen-Daniel[1], Oded Shamriz[1], Zahala Bar-On[1], Wajeeh Salaymeh[1], Amijai Saragovi[1], Ifat Abramovich[2], Bella Agranovich[2], Veronika Lutz[3], Joseph Tam[4], Anna Permyakova[4], Eyal Gottlieb[5], Magdalena Huber[3] & Michael Berger[1]

T cell activation requires a substantial increase in NAD$^+$ production, often exceeding the capacity of oxidative phosphorylation (OXPHOS). To investigate how T cells adapt to this metabolic challenge, we generate T cell-specific ADP/ATP translocase-2 knockout (Ant2$^{-/-}$) mice. Loss of Ant2, a crucial protein mediating ADP/ATP exchange between mitochondria and cytoplasm, induces OXPHOS restriction by limiting ATP synthase activity, thereby impeding NAD$^+$ regeneration. Interestingly, Ant2$^{-/-}$ naïve T cells exhibit enhanced activation, proliferation and effector functions compared to wild-type controls. Metabolic profiling reveals that these T cells adopt an activated-like metabolic program with increased mitobiogenesis and anabolism. Lastly, pharmacological inhibition of ANT in wild-type T cells recapitulates the Ant2$^{-/-}$ phenotype and improves adoptive T cell therapy of cancer in mouse models. Our findings thus suggest that Ant2-deficient T cells bypass the typical metabolic reprogramming required for activation, leading to enhanced T cell function and highlighting the therapeutic potential of targeting ANT for immune modulation.

Metabolic rewiring in T cells plays a pivotal role in regulating their activation, fate decision, and overall immune function[1–5]. Upon activation, T cells undergo substantial metabolic reprogramming to meet the increased demands for raw energy (ATP), potential energy (NAD$^+$), and biosynthetic precursors[1]. This metabolic rewiring involves the upregulation of aerobic glycolysis and oxidative phosphorylation (OXPHOS)[6]. As the metabolic hub of the cell[7], the mitochondrion undergoes extensive remodeling during activation to support anabolism, including increased biomass, morphological changes, augmented reactive oxygen species (ROS) production, and altered metabolic pathways within minutes of T cell receptor (TCR) ligation[8,9].

Rapidly proliferating cells, such as activated T cells, exhibit an elevated demand for NAD$^+$. This increased NAD$^+$ requirement presents a significant metabolic bottleneck as NAD$^+$ regeneration is intrinsically linked to ATP production via OXPHOS. The rate-limiting step in this process is the activity of ATP synthase, which dictates the pace of NAD$^+$ regeneration. Consequently, OXPHOS' capacity to meet the heightened NAD$^+$ demands of these cells is constrained, resulting in OXPHOS insufficiency[10].

---

[1]The Institute for Medical Research Israel-Canada (IMRIC), Faculty of Medicine, The Hebrew University of Jerusalem, Jerusalem, Israel. [2]Ruth and Bruce Rappaport Faculty of Medicine, Technion - Israel Institute of Technology, Haifa, Israel. [3]Institute of Systems Immunology, Philipps University of Marburg, Marburg, Germany. [4]Obesity and Metabolism Laboratory, The Institute for Drug Research, School of Pharmacy, Faculty of Medicine, The Hebrew University of Jerusalem, Jerusalem, Israel. [5]Department of Cancer Biology, University of Texas MD Anderson Cancer Center, Houston, TX, USA.
e-mail: michaelb@ekmd.huji.ac.il

Our previous findings indicate that in effector T cells, OXPHOS primarily supports anabolic tricarboxylic acid (TCA) cycle by NADH oxidation, rather than ATP production, emphasizing the critical role of NAD$^+$ regeneration[11]. This is supported by the observation that T cells can function under hypoxic conditions[12,13], indicating that mitochondrial ATP (mtATP) generation is dispensable for T cell functions. To understand how T cells adapt to this metabolic bottleneck, we focused on naïve T cells. We hypothesized that these cells might employ specific strategies to maintain cellular homeostasis under conditions of constrained OXPHOS, which may influence the transition to an activated state.

To evaluate this possibility, we indirectly induced chronic OXPHOS restriction by generating T cell-specific ADP/ATP translocase-2 knockout (Ant2$^{-/-}$) mice. Ant2, encoded by the *Slc25a5* gene, transports ADP/ATP between the mitochondria and the cytosol, maintaining mitochondrial membrane potential ($\Delta\Psi$), and supporting cellular energy homeostasis[14,15]. Ant2 deficiency reduces mtATP transfer to the cytosol, accompanied by a concomitant decrease in ADP concentrations within the mitochondrial matrix[16]. Consequently, ATP-synthase is unable to dissipate the ΔΨ due to reduced ADP availability. This sustained perturbation negatively affects the efficiency of the electron transport chain (ETC), thereby restricting OXPHOS and NAD$^+$ regeneration, effectively mimicking the OXPHOS insufficiency experienced by activated T cells. By studying these cells, we aimed to determine whether and how these adaptations influence subsequent activation and effector functions.

This study demonstrates that T cell-specific Ant2 knockout induces an activated-like metabolic program in naïve T cells, characterized by increased mitobiogenesis and anabolism, which enhances their activation propensity and effector functions. Pharmacological inhibition of ANT in wild-type T cells recapitulates these effects, improving their anti-tumor activity in vivo. These findings suggest that Ant2 deficiency bypasses typical metabolic reprogramming during T cell priming, leading to an enhanced activation state and highlighting the potential for therapeutic interventions targeting mitochondrial metabolism to modulate immune responses.

Results

Ant2$^{-/-}$ leads to T-cell lymphopenia due to failure to respond to homeostatic expansion signals

To test the impact of depleting mitochondrial ATP from T cells, we generated T-cell-specific Ant2$^{-/-}$ mice by crossbreeding Ant2$^{flox/flox}$ mice with distal Lck-cre transgenic mice (dLck-Cre$^+$). The resulting mice, referred to as Ant2$^{-/-}$, had *Slc25a5* E2+3 deleted in CD3$^+$ cells, confirmed through polymerase chain reaction (PCR) (Supplementary Fig. 1A, B). This deletion resulted in null alleles, as Ant2 mRNA was barely detectable in reverse-transcriptase PCR (RT-PCR) (Supplementary Fig. 1C). Notably, Ant1 mRNA levels remained similar between Ant2$^{-/-}$ and WT cells. Immunoblot analysis using an anti-Ant2 antibody further confirmed the absence of Ant2 protein expression in Ant2$^{-/-}$ T cells (Supplementary Fig. 1D).

To investigate the immunological effects of Ant2 deficiency, we conducted immunophenotyping using flow cytometry. Reduced percentages and counts of CD4$^+$ and CD8$^+$ T cells were evident in both the spleen (Fig. 1A, B) and lymph nodes (Supplementary Fig. 1E, F). In addition, Ant2$^{-/-}$ CD4$^+$ and CD8$^+$ T cells showed an increase in the memory-like subpopulations, characterized by elevated levels of CD44$^+$CD62L$^+$ (Supplementary Fig. 1G-J) and CD44$^+$CD122$^+$ (Supplementary Fig. 1K–N) subpopulations, at the expense of naïve subpopulations (CD62L$^+$CD44$^-$ and CD122$^-$CD44$^-$, respectively). These results indicate that Ant2$^{-/-}$ mice exhibit T-cell lymphopenia.

To understand the underlying causes of T-cell lymphopenia in Ant2$^{-/-}$ mice, we initially examined thymic development using flow cytometry. Comparing WT and Ant2$^{-/-}$ mice, we found that the pre- and post-positive selection thymic populations, CD69$^-$TCRβ$^-$ and CD69$^+$TCRβ^{hi}, respectively, were comparable between the two groups (Fig. 1C, D)[17]. However, we observed a slight but significant decrease in the double-positive (CD4$^+$CD8$^+$) cell population and an increase in the single-positive (CD4$^+$ or CD8$^+$) cell populations in Ant2$^{-/-}$ mice (Fig. 1E, F). These findings suggest intact thymic development with a minor increase in thymic egress, which is consistent with the observed T-cell lymphopenia in Ant2$^{-/-}$ mice.

To evaluate the expansion capacity of naïve Ant2$^{-/-}$ T cells in the secondary lymphatic system, we conducted a proliferation assay in response to homeostatic expansion signals. We performed adoptive transfer experiments using CD45.2$^+$ CellTrace-labeled WT splenocytes and carboxyfluorescein diacetate succinimidyl ester (CFSE)-labeled Ant2$^{-/-}$ splenocytes. The transferred cells were introduced into sublethally irradiated syngeneic recipient mice (CD45.1$^+$). Additionally, a reciprocal experiment was conducted using CFSE-labeled WT splenocytes and CellTrace-labeled Ant2$^{-/-}$ splenocytes. Flow cytometry analysis of donor T cells was performed 7 days post-transfer (Fig. 1G). Our results demonstrate that in response to homeostatic expansion signals, Ant2$^{-/-}$ CD8$^+$ (Fig. 1H, I) and CD4$^+$ (Supplementary Fig. 1O, P) T cells exhibited significantly reduced proliferation compared to WT cells. Notably, Ant2$^{-/-}$ CD4$^+$ and CD8$^+$ T cells displayed intact CD127 (IL7-R) (Supplementary Fig. 1Q, R). Consistent with these findings, Ant2$^{-/-}$ T cells exhibited reduced proliferation potential under steady-state conditions. This was evidenced by an increased percentage of cells in the G0 phase of the cell cycle, accompanied by a decrease in the percentage of cells in the G1 phase, as determined by Ki-67 and DAPI staining, together with an overall reduction in Ki-67 expression levels (Fig. 1J, K and Supplementary Fig. 1U, V). Importantly, we found no evidence of increased cell death of Ant2$^{-/-}$ T cells, as assessed by Annexin V and propidium iodide (PI) staining (Supplementary Fig. 1S, T).

Collectively, these findings suggest that the T-cell lymphopenia observed in Ant2$^{-/-}$ mice is primarily attributed to a defect in the homeostatic expansion of naïve T cells within the secondary lymphoid organs, rather than impaired thymic development or enhanced apoptosis.

Ant2$^{-/-}$ mice demonstrate intact T-cell-dependent immunity

To assess the impact of T-cell lymphopenia on T-cell-dependent immunity in Ant2$^{-/-}$ mice, we performed several in vivo experiments. First, we assessed CD4$^+$ T-cell immunity by examining the thymus-dependent B cell antibody response and cytokine production in mice immunized with ovalbumin (OVA) (Fig. 2A)[18]. Surprisingly, the concentrations of OVA-specific IgG1 and IgG2a antibodies (Fig. 2B, C), as well as the cytokines IFN-γ and IL-4 (Fig. 2D, E), were found to be equivalent in the sera of both WT and Ant2$^{-/-}$ immunized mice.

Next, to evaluate CD8$^+$ T cell function, we intradermally injected WT and Ant2$^{-/-}$ mice with an OVA-expressing lentivirus (Lv-OVA) into the left ear pinna[11,19]. After seven days, we assessed the activation status and ratios of OVA-associated CD8$^+$ T cells (TCR Vα2$^+$) in the left deep cervical lymph nodes (LN), using the right LN as a control. Activation status was determined by staining for established in vivo activation markers, including elevation of CD44 and CD25, and reduction of CD62L. Notably, the left LN of all tested mice exhibited visible swelling and an increase in absolute cell number compared to their right LN (Supplementary Fig. 2A, B). Consistent with the observed lymphopenia, Ant2$^{-/-}$ left LN demonstrated a decrease in the total CD8$^+$ ratios compared to WT (Supplementary Fig. 2C, D). However, the percentages of OVA-associated cells (CD8$^+$Va2$^+$) were comparable between the two groups (Supplementary Fig. 2C, E). Furthermore, CD8$^+$Vα2$^+$ cells derived from Ant2$^{-/-}$ mice showed an increase in both the percentages and absolute numbers of CD62L$^-$CD44$^+$ (Fig. 2F–H) and CD62L$^-$CD25$^+$ (Fig. 2I–K) cells compared to their WT counterparts.

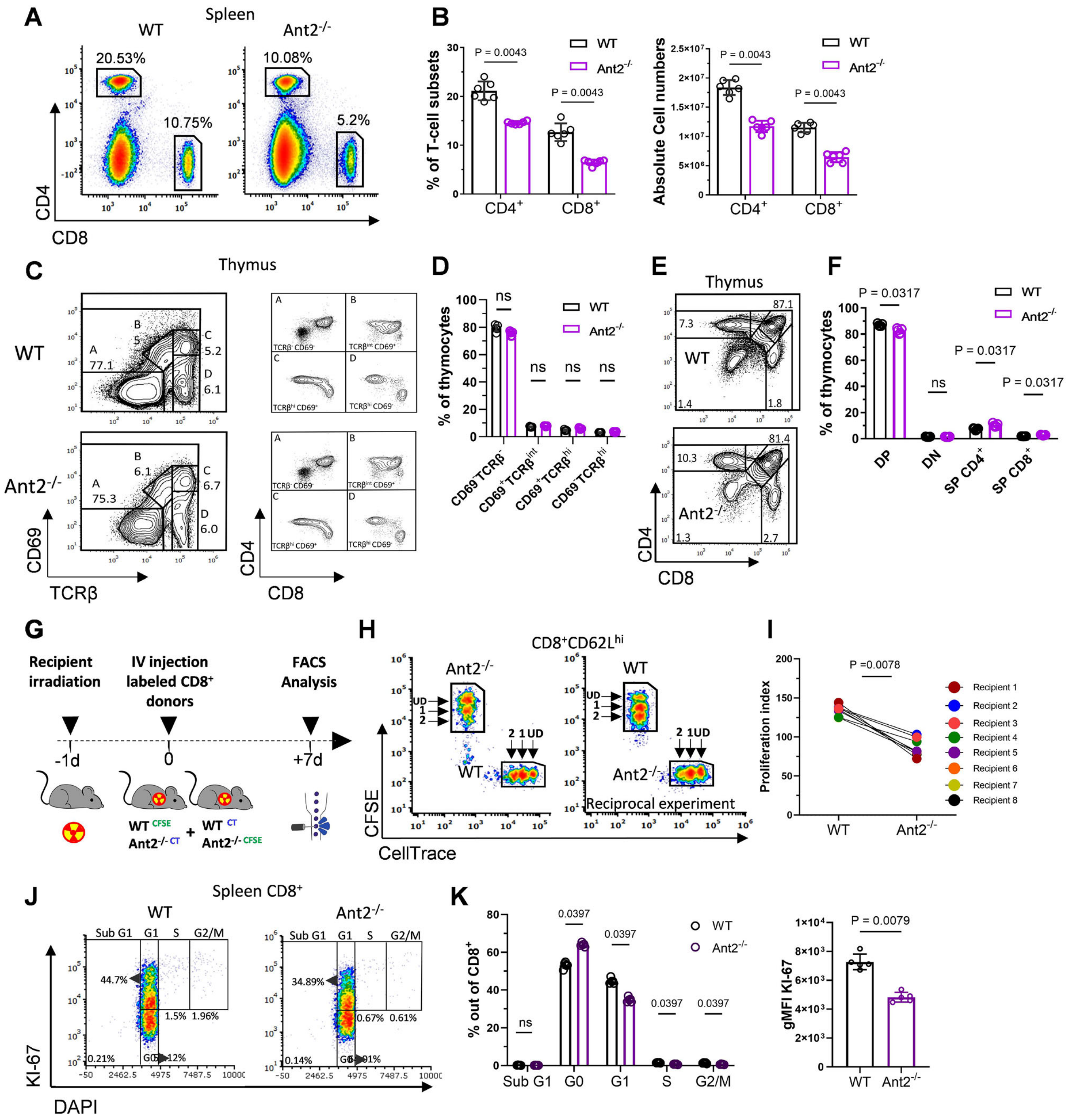

Fig. 1 | Impaired homeostatic expansion of Ant2$^{-/-}$ T cells. **A** Representative flow cytometry plots showing the frequency of CD4$^+$ and CD8$^+$ T cells in the spleen from WT and Ant2$^{-/-}$ littermate mice (6–9 weeks old). **B** Bar graphs summarizing the results in (**A**), indicating percentages **(left)** and absolute cell numbers **(right)** (n = 6). **C**–**F** Analysis of thymus development of WT and Ant2$^{-/-}$ littermate mice (6–9 weeks old). **C Left panel:** representative flow cytometry plots showing four developmental stages (**A**–**D**), distinguished by CD69 vs TCRβ staining of whole thymocytes. **Right panel:** CD4 vs. CD8 staining gated on each of the developmental stages, (**A**–**D**). **D** Bar graph summarizing the results shown in (**C**), left panel (n = 5). **E** Representative flow cytometry plots showing the frequency of CD4 vs. CD8 in the thymus-derived from 6 to 9 weeks old WT and Ant2$^{-/-}$ littermate mice. **F** Bar graph summarizing the results of panel (**F**). DP-double positive, DN-double negative, and SP-single positive. **G** Schematic of homeostatic expansion experiment; co-adoptive transfer of CFSE-labeled WT, and CellTrace-labeled Ant2$^{-/-}$ -derived splenocytes to sub-lethally irradiated recipient mice. The reciprocal experiment was also performed. **H** Representative flow cytometry plots showing CFSE vs CellTrace intensities gated on donor CD8$^+$ CD62L^{hi} T cells. **I** Graph depicting paired proliferation indexes of donor WT and Ant2$^{-/-}$ CD8$^+$ T cells (n = 8). **J**–**K** Ki-67 and cell cycle analysis of CD8$^+$ T cells (**J**) Representative flow cytometry plots of DAPI vs Ki-67 gated on CD8$^+$ T cells. **K** Bar graphs summarizing the results in (**J**), as the percentages of cells in each of the cell cycle stages **(left)** and total gMFI of Ki-67 **(right)** (n = 5). Statistical method: Two-tailed Mann–Whitney test (**B**, **D**, **F**, **K**), or two-tailed Wilcoxon matched-pairs signed rank test (**I**). Data are represented as mean ± S.D. *n* refers to the number of biologically independent samples. ns = not significant. Source data are provided as a Source Data file.

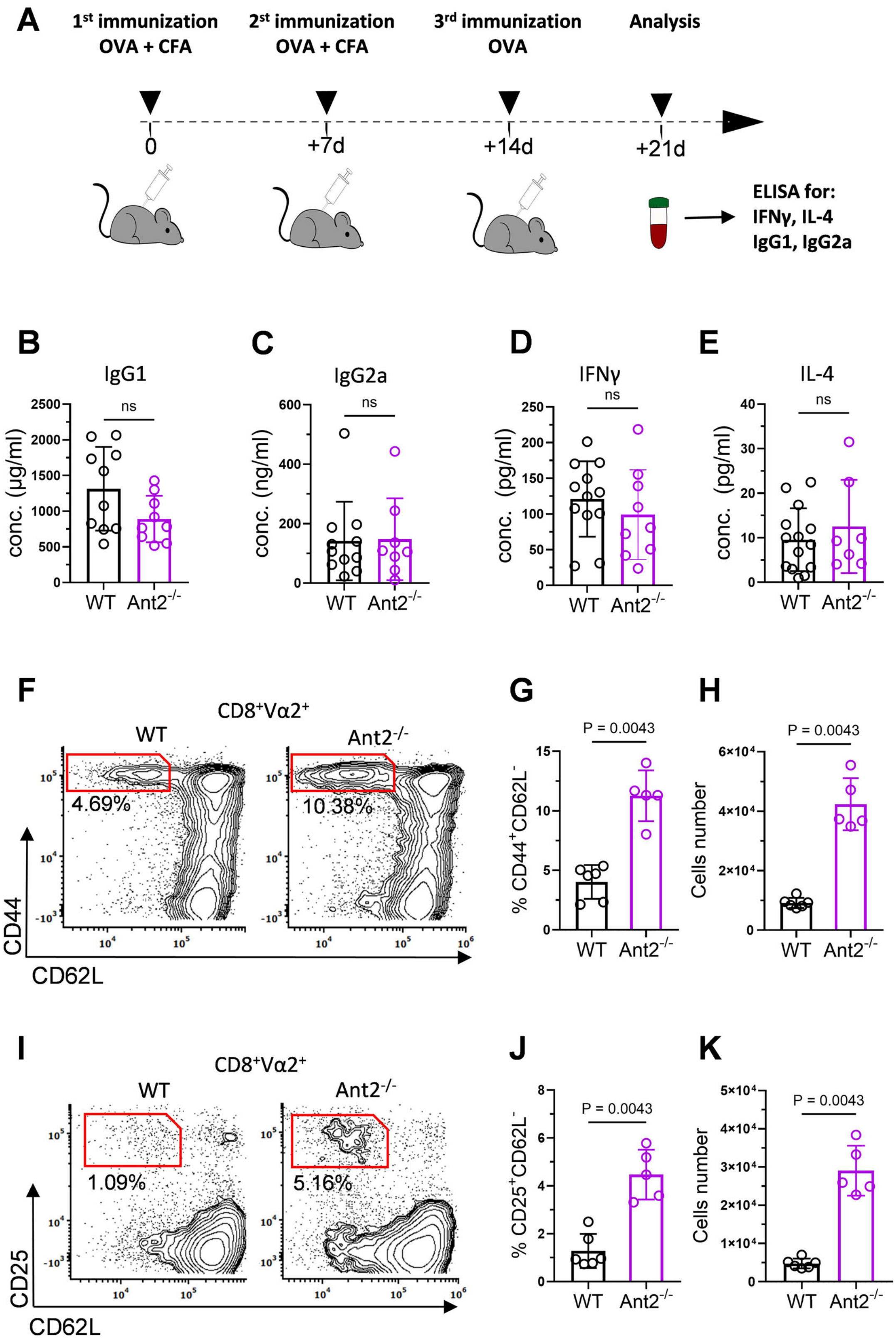

In summary, our findings indicate that the observed lymphopenia in Ant2$^{-/-}$ mice does not significantly impact their T cell-dependent immune responses. Instead, we observed an increase in effector markers in CD8^{+} T cells. This increase in activation markers may explain the intact concentrations of cytokines in the sera of Ant2$^{-/-}$ mice, suggesting T-cell hyperresponsiveness as a compensatory mechanism to preserve T-cell-dependent immunity.

Ant2$^{-/-}$ T cells have a higher propensity to activation stimuli and improved effector functions

Based on our in vivo results, we hypothesized that Ant2$^{-/-}$ T cells might demonstrate increased sensitivity to activation cues and heightened effector functions. To test our hypothesis, we performed a series of in vitro experiments. We examined their response to different concentrations of αCD3/αCD28 antibodies to assess their response to

Fig. 2 | Intact T-cell mediated immunity in Ant2$^{-/-}$ mice. **A** Schematic representation of the immunization experiment used to estimate CD4$^+$ T-cell responses. WT and Ant2$^{-/-}$ mice were immunized three times at 7-day intervals. The first two immunizations included OVA protein in complete Freund's adjuvant (CFA), while the third included OVA without CFA. One week after the third injection the concentration of, OVA-specific IgG1 (WT; n = 10, Ant2$^{-/-}$; n = 9) (**B**) and IgG2a (WT; n = 11, Ant2$^{-/-}$; n = 8) (**C**), as well as the cytokines IFNγ (WT; n = 12, Ant2$^{-/-}$; n = 9) (**D**) and IL-4 (WT; n = 14, Ant2$^{-/-}$; n = 7) (**E**), were measured in the serum of the mice using enzyme-linked immunosorbent assay (ELISA). **F**–**K** WT and Ant2$^{-/-}$ littermate mice were primed intradermally in the left ear-pinna with 5 × 10^6 transduction units (TU) of lentivirus expressing OVA (LvOVA). Seven days post-infection, cervical lymph nodes (LN) were dissected, and single cells were stained for activation-related surface markers. **F** Representative flow cytometry plots showing CD62L vs. CD44 gated on CD8$^+$Vα2$^+$ T cells. **G** Bar graph summarizing the results shown in F (WT; n = 6, Ant2$^{-/-}$; n = 5). **H** Absolute cell number of CD8$^+$Vα2$^+$CD44$^+$CD62L$^-$ in the cervical LN of WT and Ant2$^{-/-}$ mice. **I** Representative flow cytometry plots showing CD62L vs. CD25 gated on CD8$^+$Vα2$^+$ T cells. **(J):** Bar graph summarizing the results shown in (**I**) (WT; n = 6, Ant2$^{-/-}$; n = 5). **K** Absolute cell number of CD8$^+$Vα2$^+$CD25$^+$CD62L$^-$ in the cervical LN of WT and Ant2$^{-/-}$ mice. Statistical method: Two-tailed Mann–Whitney test. Data are represented as mean ± S.D. *n* refers to the number of biologically independent samples. ns = not significant. Source data are provided as a Source Data file.

activation stimulus. Activated Ant2$^{-/-}$ CD8$^+$ T cells exhibited enhanced proliferation capacity (Fig. 3A, B) and CD25 expression (Fig. 3C, D) compared to their WT counterpart across all tested concentrations of αCD3/αCD28 antibodies. Moreover, we observed a significant increase in both the proportions of IFNγ$^+$ cells within the total CD8$^+$/CD25$^+$ T cells and the IFNγ intensity per cell in Ant2$^{-/-}$ CD8$^+$ T cells compared to WT controls (Fig. 3C, E, F).

These results suggest that Ant2$^{-/-}$ CD8$^+$ T cells exhibit an increased propensity for activation, as well as enhanced effector functions.

In an effort to investigate peptide-specific T-cell responses, we generated OT-I/Ant2$^{-/-}$ mice and compared their responses to those of OT-I/WT littermates[20]. Noteworthy, the OT-I model did not ameliorate the lymphopenia resulting from Ant2 deficiency (Supplementary Fig. 3A, B). To compare peptide-specific response while minimizing potential lymphopenia-related effects, we conducted a co-culture experiment. To distinguish between T cell populations, CFSE-labeled OT-I/WT and CellTrace-labeled OT-I/Ant2$^{-/-}$ splenocytes were co-cultured in approximately a 1:1 ratio of CD8$^+$ T cells (Supplementary Fig. 3C). These co-cultured cells were subsequently activated with OVA-peptide (SIINFEKL) for 24 h. Our findings replicated our prior results using antibody activators and demonstrated that OT-I/Ant2$^{-/-}$ CD8$^+$ T cells exhibited significantly higher percentages of CD25$^+$IFNγ$^+$ cells and increased IFNγ intensity per cell (Supplementary Fig. 3D, E) compared to their WT counterparts. To further examine the effector function, we assessed the cytotoxic activity of OT-I/Ant2$^{-/-}$ CD8$^+$ effector T cells in an in vitro killing assay[21]. B16 melanoma cells expressing OVA (B16-OVA) and control cells (B16) were incubated with either OT-I/WT or OT-I/Ant2$^{-/-}$ CD8$^+$ effector T cells for 6 h. The survival of B16-OVA cells incubated with Ant2$^{-/-}$ derived CD8$^+$ effector T cells was significantly lower compared to WT cells (Fig. 3G). These results highlight the enhanced cytotoxic capacity of Ant2$^{-/-}$ CD8$^+$ T cells in an in vitro setting, suggesting their enhanced ability to eliminate target cells.

To support our in vitro findings, we examined the proliferation of OT-I/Ant2$^{-/-}$ CD8$^+$ T cells upon activation in vivo. CellTrace-labeled CD8$^+$ T cells from CD45.2 OT-I/WT or OT-I/Ant2$^{-/-}$ mice were intravenously transferred into CD45.1 WT recipient mice. One day after, the recipient mice were intraperitoneally injected with 30 μg of OVA. Three days after cell transfer, splenocytes were harvested from the recipient mice and analyzed for CellTrace intensity. Consistent with our in vitro findings, Ant2$^{-/-}$ CD8$^+$ T cells exhibited an increased proliferation in vivo (Fig. 3I, J).

In summary, our results demonstrate that naïve Ant2$^{-/-}$ CD8$^+$ T cells, in contrast to WT cells, exhibit decreased proliferation capacity during homeostatic expansion. Concurrently, they display an elevated propensity to activation signals, alongside improved proliferation capabilities and enhanced effector functions.

Increased mitochondria biomass and spare respiratory capacity in Ant2$^{-/-}$ T cells

The mitochondria play a central role in cellular metabolism and energy production, making them vital for T-cell activation and effector functions[22,23]. Considering its pivotal role in the ADP/ATP exchange between the mitochondria and the cytosol, Ant2 deficiency leads to a decrease in mitochondria-derived ATP levels in the cytosol. Simultaneously, it causes a reduction in ADP levels in the mitochondrial matrix[16]. Since ADP concentration drives ATP-synthase complex activity, its decrease reduces this activity, triggering proton accumulation in the intermembrane space. Consequently, this leads to increased ΔΨ, which can ultimately inhibit to an inhibition of oxidative phosphorylation (OXPHOS)[24,25]. Indeed, naïve Ant2$^{-/-}$ CD8$^+$ and CD4$^+$ T cells displayed substantially increased *ΔΨ*, as shown by Tetramethylrhodamine, methyl ester (TMRM) staining (Fig. 4A, B and Supplementary Fig. 4A, B).

To assess the impact of Ant2 deficiency on mitochondrial biomass, we crossbred Ant2$^{-/-}$ mice with those carrying the mitochondria-specific fluorescent protein Dendra2 (mtDendra2). mtDendra2 protein is expressed in all tissues, allowing live-cell imaging, and its intensity correlates with mitochondrial mass[26]. By utilizing flow cytometry, we quantified the intensity of mtDendra2 in CD8$^+$ T cells during various stages of in vitro activation. Naïve and activated Ant2$^{-/-}$ CD8$^+$ T cells showed increased intensity per cell compared to WT cells, indicating higher mitochondrial content (Fig. 4C).

In addition, to corroborate the association between the increase in mitochondrial biomass and Cre-mediated Ant2 deletion, we assessed mtDendra2 intensity in thymocytes across different developmental stages, both pre- and post- cre-mediated deletion, as well as in mature T cells within the spleen. Cre-mediated deletion by the dLck-promoter takes place as early as in the TCRβ selection stage (TCRβ^{int}), reaching its peak at the TCRβ^{hi} stage[27]. Intriguingly, when comparing the ratio of mtDendra2 intensity between Ant2$^{-/-}$ and WT T cells at each developmental stage, a notable surge in mitochondrial biomass was observed precisely at the TCRβ^{hi} stage. This augmentation was further amplified in mature splenic CD8$^+$ T cells within the Ant2$^{-/-}$ mice (Supplementary Fig. 4C, D). Collectively, these results support the notion that the loss of Ant2 is correlated with a significant increase in mitochondrial biomass over time. Furthermore, mitochondrial DNA copy number was assessed using RT-qPCR by comparing the ratio of two target mitochondrial genes, *Mt-rnr2* (mitochondrially encoded 12S rRNA) and *Mt-co1* (mitochondrially encoded cytochrome c oxidase I), to a reference nuclear gene, *B2m* (beta-2-microglobulin). Naïve and activated Ant2$^{-/-}$ CD8$^+$ T cells exhibited higher mitochondrial DNA copy number compared to WT cells (Fig. 4D–F). Together, these findings strongly suggest that Ant2 loss in naïve T cells results in increased mitochondrial content.

We then examined the effect of Ant2 deficiency on the mitochondrial function of CD8$^+$ T cells. Using Seahorse analysis[28], we compared the oxygen consumption rate (OCR) of naïve and activated CD8$^+$ T cells from both WT and Ant2$^{-/-}$ mice. The basal OCR of naïve and activated Ant2$^{-/-}$ CD8$^+$ T cells was similar to that of their WT counterparts (Fig. 4G, H, J, K). These data suggest that, despite increased mitochondrial mass, the basal OCR per mitochondrion is reduced in Ant2$^{-/-}$ T cells compared to WT controls. Interestingly, when treated with the uncoupler FCCP, which dissipates membrane hyperpolarization, naïve and activated Ant2$^{-/-}$ CD8$^+$ T cells exhibited a significant increase in maximal OCR compared to WT cells, resulting in

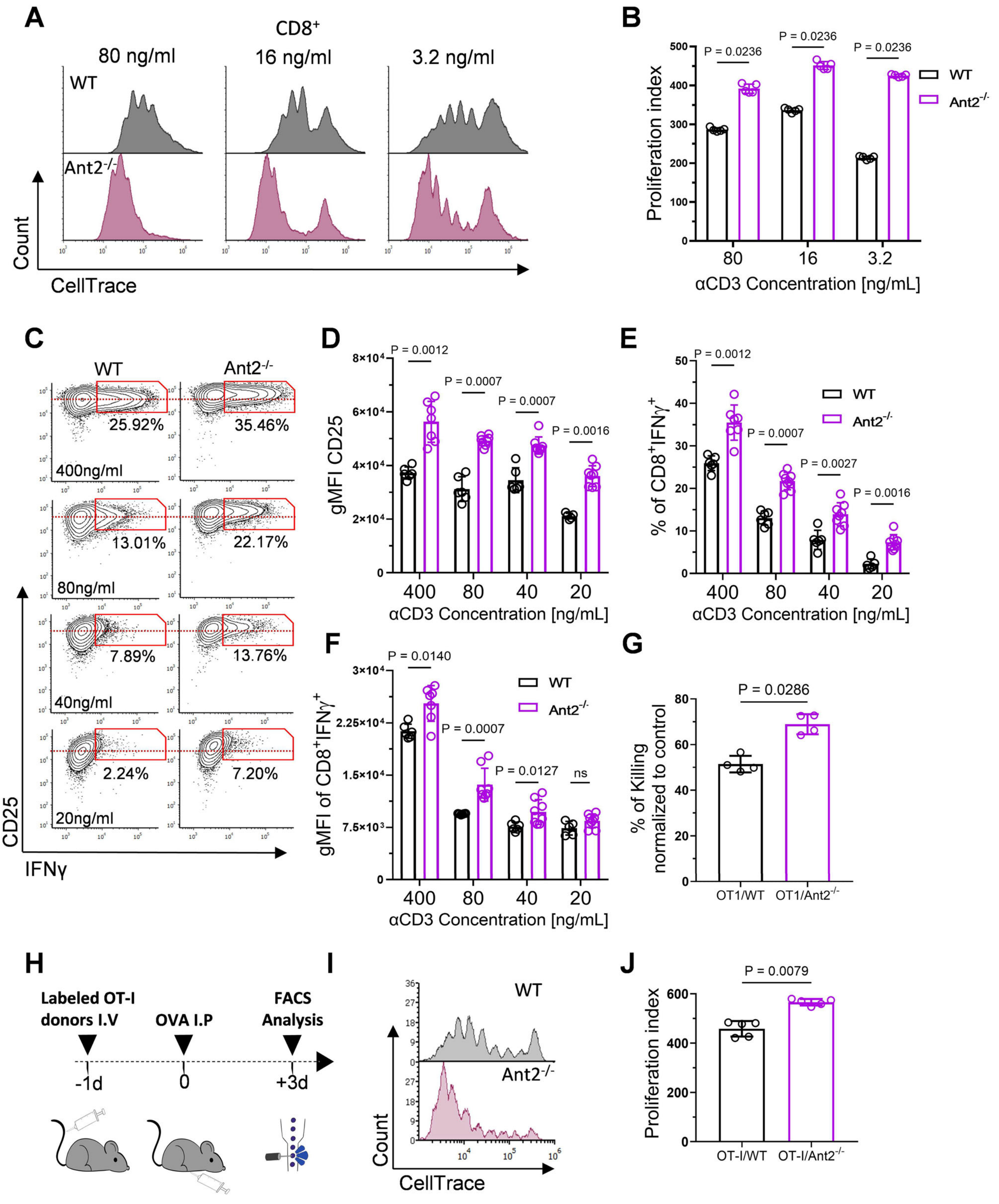

an increased spare respiratory capacity (SRC) (Fig. 4I, L)[29]. SRC provides the ability to meet increased energy demands that exceed basal requirements. Thus, we propose that the increase in mitochondrial biomass and SRC observed in Ant2-deficient T cells is a compensatory response to OXPHOS restriction.

Given the observed OXPHOS restriction and altered mitochondrial function, we next examined how Ant2 deficiency affected mitochondrial ROS (mtROS) production and mitochondrial morphology, both of which are sensitive to changes in OXPHOS[30,31]. We hypothesized that the OXPHOS inhibition imposed by the loss of Ant2 would affect mtROS generation and, consequently, alter mitochondrial morphology. Indeed, MitoSOX staining revealed that during the naïve state, Ant2$^{-/-}$ CD8^{+} T cells display a modest, yet significant increase in ROS production compared to their WT counterparts. Upon 1 h of stimulation, both Ant2$^{-/-}$ CD4^{+} and CD8^{+} T cells exhibit a further amplification of ROS production (Fig. 4M–P, Supplementary Fig. 4E, F). Consistent with these findings, our high-resolution live cell microscopy revealed that the mitochondria of naïve Ant2$^{-/-}$ CD8^{+} T cells

Fig. 3 | Increased activation potential and effector functions of Ant2$^{-/-}$ CD8$^+$ T cells. A Representative flow cytometry histograms of CellTrace intensity gated on CD8$^+$ T cells derived from WT or Ant2$^{-/-}$ mice, 72 h post-activation with the indicated concentrations of αCD3 antibody and half the amount of αCD28 antibody. **B** Bar graph summarizing the results in A as a proliferation index (n = 5). **C** Representative flow cytometry histograms showing intracellular IFNγ vs. CD25 gated on CD8$^+$ T cells derived from WT or Ant2$^{-/-}$ mice, 24 h post-activation with the indicated concentrations of αCD3 antibody and half amount of αCD28. **D**–**F** Bar graphs summarizing the results shown in (**C**) (WT; n = 6, Ant2$^{-/-}$; n = 8), as geometric mean fluorescence intensity (gMFI) of CD25 (**D**), the frequency of CD8$^+$IFNγ$^+$ T cells (**E**), and gMFI of IFNγ gated on CD8$^+$IFNγ$^+$CD25$^+$ (**F**). **G** Graph depicts the percentage of killed target B16-OVA melanoma cells after a 6-h incubation at a 1:1 ratio with WT or Ant2$^{-/-}$ OT-I CD8$^+$ T cells activated for 5 days. Target cell viability was assessed using an MTT assay after three washes with PBS (n = 4). **H** Schematic of the adoptive transfer experiment testing activation of naïve CD8$^+$ T cells. CD45.1$^{+/+}$ WT recipient mice were intravenously administered CellTrace-labeled CD45.2$^{+/+}$ T cells derived from WT or Ant2$^{-/-}$ OT-1 mice. After one day, recipient mice were intraperitoneally injected with 50 μg of OVA. On day three following cell transfer splenocytes from the mice were examined by flow cytometry for CellTrace intensity. **I** Representative flow cytometry histograms of CellTrace intensity gated on donor (CD45.2$^{+/+}$) CD8$^+$ T cells. **J** Graph depicting the proliferation index of donor WT and Ant2$^{-/-}$ OT-I T cells (n = 5). Statistical method: Two-tailed Mann–Whitney test. Data are represented as mean ± S.D. *n* refers to the number of biologically independent samples. ns = not significant. Source Data are provided as a Source Data file.

exhibited significantly higher circularity scores and lower length scores compared to WT cells (Fig. 4Q, S), indicative of fragmented mitochondrial morphology associated with increased ROS within the mitochondria[32].

Altogether, our results support the concept that Ant2 deficiency leads to decreased OXPHOS, an inherent increase in ROS generation, and alterations in mitochondrial morphology. In response to this respiratory bottleneck, Ant2$^{-/-}$ T cells increase their mitochondrial content and rewire mitochondrial function.

Activated-like proteome and distinct mitochondria in naïve Ant2$^{-/-}$ CD8$^+$ T cells

To gain insights into the metabolic changes associated with Ant2 deficiency in naïve CD8$^+$ T cells, we employed protein mass spectrometry (MS) to examine alterations in the cellular proteome. Although comparative analysis revealed that the protein expression profiles of naïve Ant2$^{-/-}$ CD8$^+$ T cells were largely similar to WT cells (Supplementary Fig. 5A), 412 proteins were upregulated and 610 were downregulated in Ant2$^{-/-}$ cells compared to WT cells (Supplementary Fig. 5B). Focusing on the 535 mitochondrial-associated proteins detected in our experiment[33], we identified 56 enriched mitochondrial proteins in Ant2$^{-/-}$ cells vs. 15 in WT (Fig. 5A, proteins marked in red). Of note, consistent with the findings of unaltered Ant1 mRNA expression levels (Fig. 1C), there was no significant change observed in Ant1 protein expression levels (Fig. 5A).

Further, in line with increased mitochondrial content, we observed elevated expression of voltage-dependent anion-selective channel protein 1 (VDAC1), indicating increased mitochondrial biomass, and key mitochondrial biogenesis proteins, including mitochondrial transcription factor A (TFAM) and deoxyguanosine kinase (DGUOK) (Supplementary Fig. 5C)[34,35]. Principal component analysis (PCA) of mitochondrial proteins revealed distinct mitochondrial proteomes between the two groups (Fig. 5B). Thus, in addition to increased mitochondrial content, Ant2$^{-/-}$ T cells exhibit distinct mitochondria.

An in-depth analysis of the proteomic data revealed several upregulated metabolic pathways in Ant2$^{-/-}$ CD8$^+$ T cells, both in mitochondrial and cytosolic compartments. The most significant upregulated pathways were OXPHOS-related proteins (such as NDUFB9, SDH, UQCRFS1, COX6C, and ATP5K, which constitute representative proteins of complex (C)I, CII, CIII, CIV, and CV, respectively) and TCA cycle-related proteins (including CS, IDH2, and FH) (Fig. 5C). These pathways play critical roles not only in adapting to insufficient OXPHOS but also in supporting T-cell activation and effector functions[23,36]. In addition, our MS analysis revealed the upregulation of crucial detoxification mechanisms. The observed adaptation resembles that of activated T cells and involves the upregulation of key antioxidant enzymes such as SOD2, catalase, and thioredoxin, along with the enhancement of the glutathione system (Fig. 5D)[37,38]. These results are in line with our increased MitoSOX staining in Ant2$^{-/-}$ T cells and suggest an attempt to maintain redox homeostasis. Additionally, the proteomic analysis uncovered alterations in other key enzymes that are typically upregulated upon activation. For example, we observed changes in proteins related to folate-dependent one-carbon metabolism (Supplementary Fig. 5D)[9,39,40], iron and heme metabolism (Supplementary Fig. 5E)[41–44], and the pentose phosphate pathway (PPP) (Supplementary Fig. 5F, G). Finally, pathway enrichment analysis conducted on all upregulated proteins in Ant2$^{-/-}$ T cells using Metascape[45], confirmed a significant enrichment of pathways associated with mitochondrial functions (Supplementary Fig. 5H).

Overall, our proteomic analysis offers critical insights into the metabolic adaptations occurring in Ant2$^{-/-}$ naïve T cells, supporting the notion that the observed mitochondrial alterations involve both increased mitobiogenesis and reprogramming.

Specialized mitochondria and activated-like metabolic signature in naïve Ant2$^{-/-}$ CD8$^+$ T cells

Next, we postulated that the observed alterations in the proteome and mitochondrial reprogramming in naïve T cells lacking Ant2 would result in a rewired glucose metabolism, ultimately contributing to the enhanced phenotype upon activation. Therefore, we cultured OT-I/WT and OT-I/Ant2$^{-/-}$ naïve CD8$^+$ T cells with $^{13}C_6$-glucose for 4 h and analyzed both the cellular and media fractions using liquid chromatography-mass spectrometry (LC-MS). This approach allowed us to assess the incorporation of ^{13}C into central metabolites and provide a comprehensive understanding of the alterations in glucose metabolism resulting from Ant2 deficiency.

Naïve Ant2$^{-/-}$ CD8$^+$ T cells exhibited a marked decrease in unlabeled phosphocreatine (PCr) to creatine levels (Fig. 6A and Supplementary Fig. 6A, B). In line with this result, our proteomic data indicate elevated Creatine Kinase B (CKB) levels in naïve Ant2$^{-/-}$ CD8$^+$ T cells (Fig. 6B). CKB, the primary isoform of creatine kinase in CD8$^+$ T cells[46], catalyzes the phosphoryl transfer from ATP to creatine and vice versa. Previous studies have demonstrated that CKB is crucial for ATP buffering in activated T cells and other cells that rapidly consume ATP[46,47]. The creatine-PCr shuttle was also proposed to serve as an energy transport between subcellular sites of ATP production[48]. Consequently, we propose that the high ATP level within the mitochondrial matrix of Ant2$^{-/-}$ T cells stimulate the conversion of creatine to PCr. PCr is then transported to the cytosol and used by CKB to phosphorylate ADP to ATP, forming a circuit that enables Ant2$^{-/-}$ T cells to compensate for the lack of direct mtATP transfer.

Naïve Ant2$^{-/-}$ CD8$^+$ T cells also displayed a decreased NAD$^+$/NADH ratio (Fig. 6C). Concurrently, we observed a significant increase in cellular and media levels of labeled pyruvate m + 3, alanine m + 3, and lactate m + 3 secretion compared to the control group (Fig. 6D, H). These findings indicate a rewiring of pyruvate metabolism, likely due to OXPHOS inhibition[49]. Notably, this metabolic signature resembles that of activated T cells, whereas the demand for NAD$^+$ exceeds OXPHOS capacities[10].

The impermeability of the inner mitochondrial membrane to NAD(P)H presents a challenge in transferring reducing equivalents to the mitochondria. Consequently, mitochondria have evolved various shuttles and para-metabolic pathways to regenerate NAD$^+$ pools.

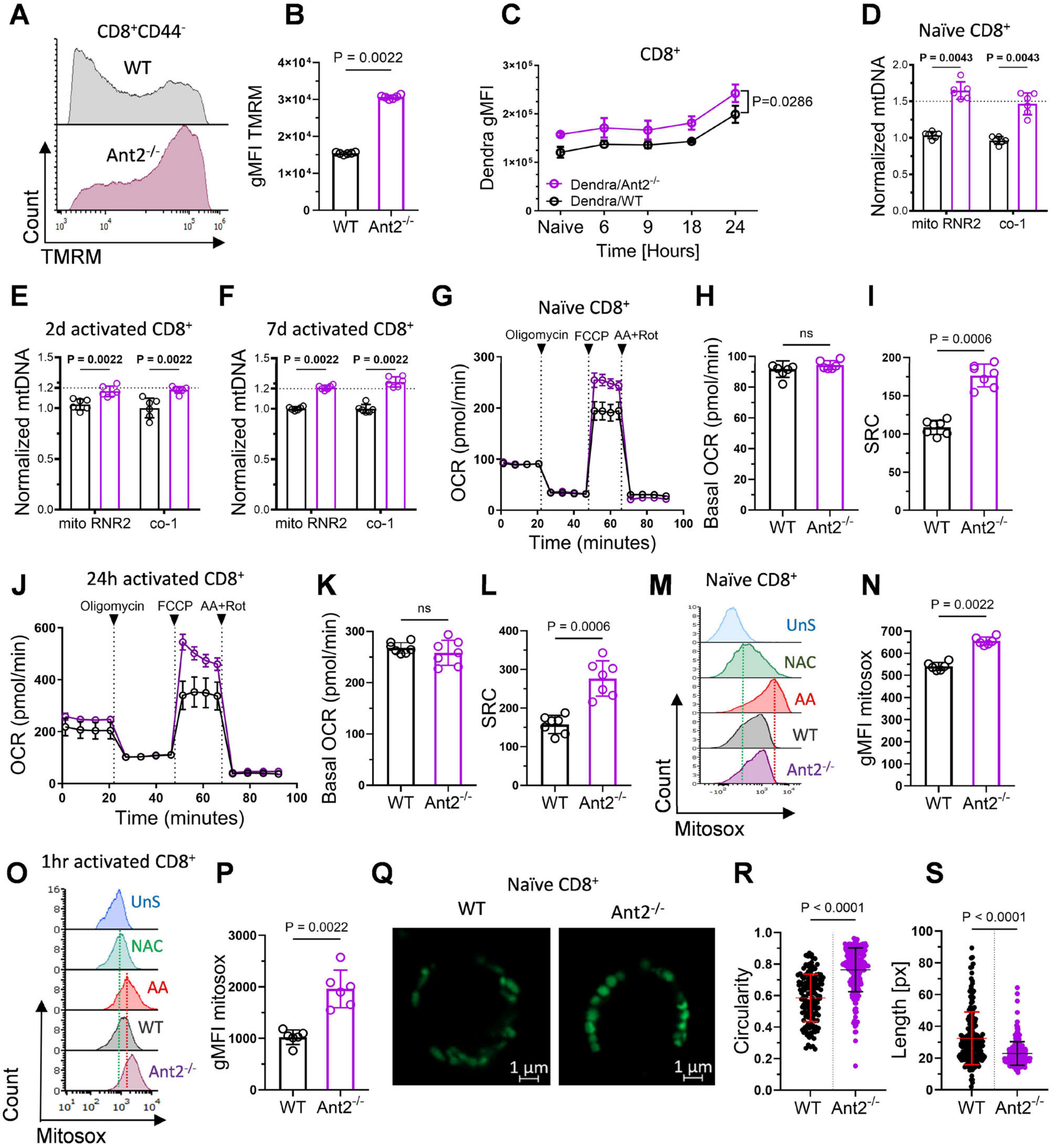

Fig. 4 | Increased biomass, and altered function, of mitochondria in Ant2$^{-/-}$ T cells. **A** Representative flow cytometry histogram of TMRM staining gated on naïve (CD44$^-$) CD8$^+$ T cells. **B** Bar graph summarizing the results shown in A (n = 6). **C** Graph summarizes mtDendra2 intensity of naïve and activated CD8$^+$ T cells derived from WT and Ant2$^{-/-}$ mito-Dendra2 mice at the indicated time points post activation (n = 4). Relative expression of mitochondrial DNA (mtDNA) in naïve (**D**), activated for 2 d (**E**) or activated for 7 d (**F**) WT or Ant2$^{-/-}$ CD8$^+$ T cells, measured by RT-PCR using 2 different set of primers targeted to amplify two independent mitochondrial genes, *Rnr2* and *Co-1*. Results were normalized to the expression of the nuclear gene, *β2m* (n = 6). **G** Continuous dot graph of oxygen consumption rate (OCR) measured by Seahorse XF96, following consecutive injections of Oligomycin [1 μM], FCCP [2 μM], Rotenone + Antimycin-A [1 μM] (AA + Rot) of isolated naïve CD8$^+$ T cell from WT (black) or Ant2$^{-/-}$ (purple) mice at the indicated time points. **H**, **I** Bar graphs summarizing the results shown in (**G**), as basal OCR (**H**) and spare respiratory capacity (SRC) (WT; n = 7, Ant2$^{-/-}$; n = 6) (**I**). SRC is calculated as the maximal OCR (after FCCP injection) minus Basal OCR. **J** Same as in G using activated CD8$^+$ T cells for 24 h. **K**, **L** Bar graphs summarizing the results shown in (**J**), as basal OCR (**K**), and SRC (**L**) (n = 7). **M**–**P** Representative flow cytometry histograms of MitoSOX staining gated on (**M**) Unstimulated (naïve) and (**O**) 1-h activated CD8$^+$ T cells (n = 6). WT CD8$^+$ T cells were used as controls, with the following conditions from top to bottom: unstained (UnS), pre-treated with 200 μM N-Acetyl Cysteine (NAC), and treated with 1 μM Antimycin A (AA). **N**, **P** Bar graphs summarizing the results of M (unstimulated) and O (stimulated) CD8$^+$CD44$^-$ T cells as gMFI of MitoSOX, respectively (**Q**–**S**) Representative live imaging of mitochondrial morphology in purified CD8$^+$ T cells derived from WT and Ant2$^{-/-}$ mitoDendra2 littermate mice. **R**–**S** Quantitative analysis of the images for measurements of mitochondria length (**R**) and circularity (**S**). Over n = 300 mitochondria were analyzed for each genotype (WT-319, Ant2$^{-/-}$ = 473). Statistical method: Two-tailed Mann–Whitney test (**B**–**F**, **H**, **I**, **K**, **L**, **N**, **P**), or unpaired t-test (**R**, **S**). Data are represented as mean ± S.D (**B**–**F**, **H**, **I**, **K**–**S**), or as mean ± SEM (**G**, **J**). *n* refers to the number of biologically independent samples. ns = not significant. Source data are provided as a Source Data file.

Proline, a non-essential amino acid derived from glutamate, has not been extensively studied of T cells. Recently, evidence resurfaced that proline biogenesis may serve as a para-metabolic pathway for regenerating mitochondrial NAD$^+$ in highly proliferative cancerous cells, where OXPHOS is insufficient to regenerate adequate NAD$^+$ levels[50–54]. Our MS-proteomics analysis revealed the upregulation of the mitochondrial enzymes involved in proline biosynthesis, pyrroline-5-carboxylate synthase (P5CS) and pyrroline-5-carboxylate reductase

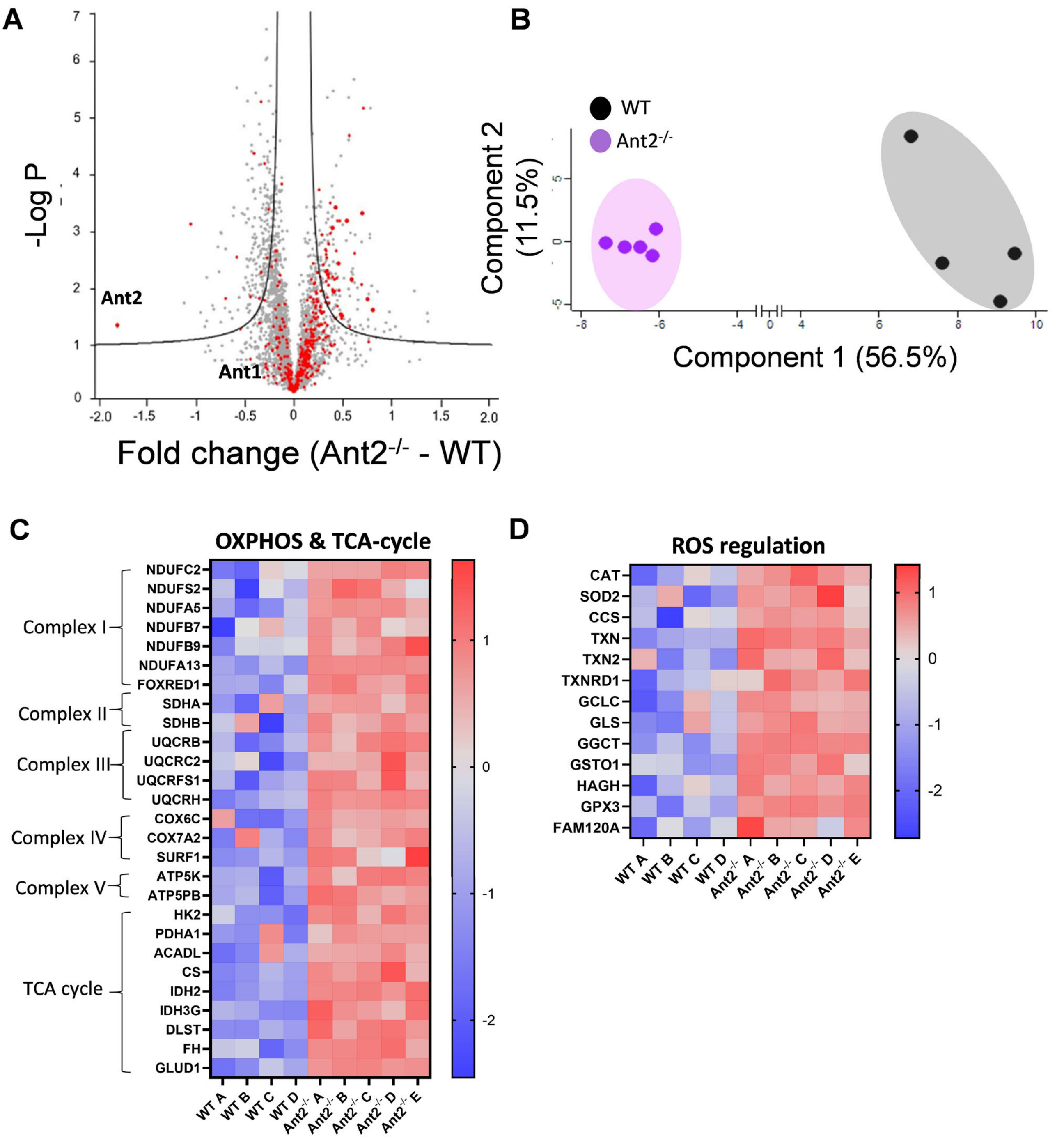

Fig. 5 | Altered proteome and distinct mitochondria in naïve Ant2$^{-/-}$ CD8$^+$ T cells. **A–D** Mass-spectrometry analysis was performed on protein extracts from naïve (CD44$^-$) CD8$^+$ T cells derived from WT or Ant2$^{-/-}$ OT-I mice (WT: n = 4, Ant2$^{-/-}$: *n* = 5). **A** Volcano plot displaying differentially expressed proteins (relative peptide abundances). The negative logarithm of statistical significance (*p value*) is plotted against the fold change magnitude. Prior to imputation from a normal distribution, Label-Free Quantitation (LFQ) levels were log$_2$-transformed. Red dots represent mitochondrial-associated proteins sourced from MitoCarta2.0. **B** Principal component analysis comparing the log$_2$-transformed data of all mitochondrial-associated proteins. The first two principal components, which capture the highest variance in the data, are depicted. Heatmaps illustrating differentially expressed proteins associated with oxidative phosphorylation and tricarboxylic acid cycle (**C**), as well as reactive oxygen species regulation and glutathione synthesis (**D**). The heatmaps were generated based on the log$_2$ fold change values of individual genes between the two compared samples. The color gradient ranges from red, indicating a significant fold change, to blue, representing a minor fold change. Statistical method: Two-tailed multiple *t*-tests, FDR < 0.05, S0 < 0.1 (**A**), or Benjamini-Hochberg method (FDR < 0.05) (**B**), or Student's *t* test analysis conducted on log$_2$-transformed data after the Z-score normalization step (**C**, **D**). Data are represented as mean ± S.D. *n* refers to the number of biologically independent samples. Source data are provided as a Source Data file.

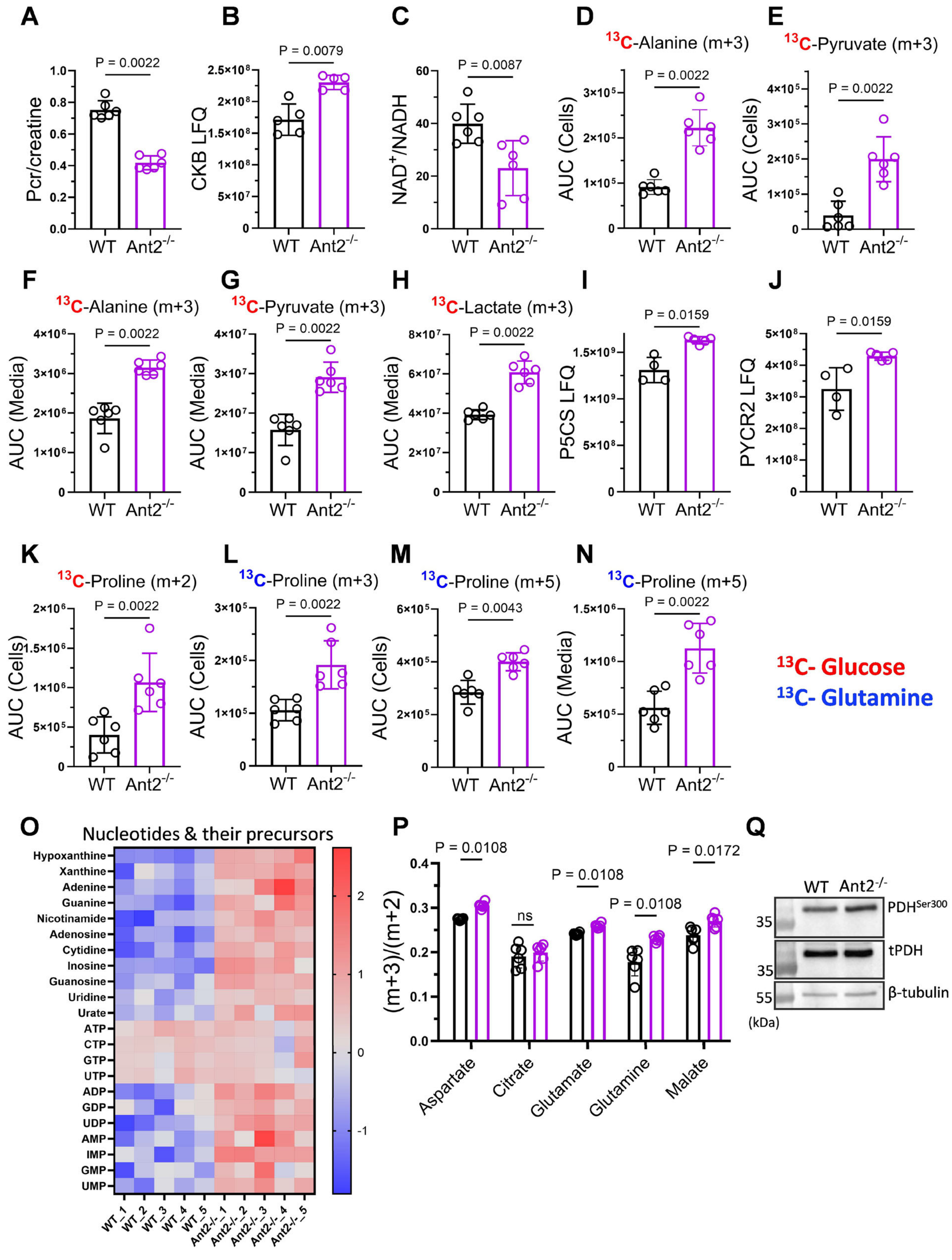

(PYCR2) (Fig. 6I, J). These enzymes catalyze the reduction of glutamate to proline by consuming NAD(P)H. Interestingly, our $^{13}C_6$-glucose-tracing experiments showed a significant increase in labeled proline m + 2 in naïve Ant2$^{-/-}$ CD8$^+$ T cells (Fig. 6K), indicating elevated proline biosynthesis even in the naïve state.

We further investigated the source of glutamate for proline biosynthesis using $^{13}C_5$-glutamine tracer analysis. In line with our glucose tracing, proline m + 3 and proline m + 5 were elevated in Ant2$^{-/-}$ CD8$^+$ T cells (Fig. 6L–M). Furthermore, a significant portion of the newly synthesized proline m + 5 was secreted from the cells (Fig. 6N). Given the catabolic in nature of naïve CD8$^+$ T cells, the secreted proline is unlikely to be used solely for protein synthesis. Rather, we propose that Ant2$^{-/-}$ naïve CD8$^+$ T cells engage in proline biosynthesis as a parametabolic pathway to regenerate mitochondrial NAD(P)$^+$. This is

Fig. 6 | Metabolomic adaptations of naïve Ant2$^{-/-}$ CD8$^+$ T cells. A–O Comparison of area under the curve (AUC) values from metabolomics analysis using $^{13}C_6$-glucose (red) or $^{13}C_5$-glutamine (blue) tracing alongside Label-Free Quantitation (LFQ) values from proteomics analysis in naïve (CD44$^-$) WT and Ant2$^{-/-}$ CD8$^+$ T cells. **A** Bar graph showing the ratio between the AUC values of unlabeled Phosphocreatine (Pcr) and Creatinine (n = 6). **B** Bar graph displaying the LFQ values of Creatine Kinase (WT: n = 4, Ant2$^{-/-}$: n = 5). **C** Bar graph demonstrating the NAD$^+$/NADH ratio (n = 6). **D–H** LC-MS measurements of labeling patterns for glycolytic derivatives after [$^{13}C_6$]-glucose tracing. Bar graphs **display** AUC values of alanine m + 3 (**D**, **F**), and pyruvate m + 3 (**E**, **G**) in the cell and media fractions, respectively, and lactate m + 3 in the media fraction (n = 6) (**H**). Bar graphs showing LFQ values of P5CS (**I**) and PYCR2 (**J**) (WT: n = 4, Ant2$^{-/-}$: *n* = 5). **K–N** Bar graphs displaying AUC from LC-MS measurements of proline labeling patterns (n = 6). **K** Bar graph showing AUC values for $^{13}C_6$-glucose-derived proline (m + 2) in the cell fraction. **L**, **M** Bar graphs showing AUC values for $^{13}C_5$-glutamine-derived proline (m + 3 and m + 5) in the cell and media fraction, respectively, and AUC values for proline (m + 5) in the media fraction (**N**). **O** Heatmap illustrating differentially expressed unlabeled nucleotides and their precursors. The heatmap was generated based on the log2 fold change of individual metabolites (n = 5). **P** Bar graphs illustrating the (m + 3) to (m + 2) ratio of specific TCA-cycle intermediates and TCA-cycle-derived metabolites in naïve (CD44$^-$) WT and Ant2$^{-/-}$ CD8$^+$ T cells (n = 6). **Q** Representative immunoblot analysis of whole-protein extracts from purified WT and Ant2$^{-/-}$ CD8$^+$ cells using anti-tPDH and pPDHser300 antibodies. Anti-tubulin was used as a loading control (pooling of n = 3). Statistical method: two-tailed Mann–Whitney test (**A–N**, **P**), or Student's *t* test analysis conducted on log$_2$-transformed data after the Z-score normalization step (**O**). Data represented as the mean ± S.D. *n* refers to the number of biologically independent samples. ns = not significant. Source data are provided as a Source Data file.

further supported by our glucose tracing, which revealed increased PPP activity[55], as indicated by elevated levels of unlabeled nucleotides and their precursors (Fig. 6O). Additionally, specific labeled metabolites, such as inosine m + 5 and ATP m + 5, provide additional indications of increased nucleotide metabolism in Ant2$^{-/-}$ CD8$^+$ T cells (Supplementary Fig. 6C, D). These findings highlight the multifaceted metabolic adaptations in Ant2-deficient T cells aimed at maintaining redox homeostasis.

Despite constrained OXPHOS, we observed no signs of TCA cycle congestion in these cells, as the labeling patterns of TCA cycle intermediate metabolites remained comparable to WT cells (Supplementary Fig. 6E–H). In fact, we observed upregulation of labeled TCA cycle-derived amino acids (Fig. 6K, L, and Supplementary Fig. 6I–L), indicating an enhanced cataplerosis[36,56].

Cataplerosis, the process of carbon exiting the TCA cycle for precursor generation, is known to occur during T-cell stimulation, enabling the cells to generate macromolecules for proliferation[57]. Given the observed increase in carbon efflux in naïve Ant2$^{-/-}$ CD8$^+$ T cells, there must be a corresponding increase in carbon influx, termed anaplerosis, to compensate for the lost carbon[36]. Our glutamine tracing experiments exclude glutamine as an anaplerotic source (Fig. 6L–N and Data Source file), which is expected as glutamine addiction occurs upon activation. Thus, we explored an alternative anaplerosis source.

Pyruvate carboxylase (PC) converts pyruvate to oxaloacetate, replenishing the TCA cycle with a 4-carbon input instead of the typical 2-carbon input (acetyl-CoA), mediated by pyruvate dehydrogenase (PDH). PC activity is critical for activated T-cell proliferation and eliciting anti-tumor responses in-vivo[58,59]. While direct measurement of PC activity is challenging, indirect activity can be inferred from certain conditions and measurements. First, we anticipated increased PC activity due to inhibited OXPHOS and increased ROS production, as previous studies have demonstrated their correlation[60]. Secondly, leveraging our $^{13}C_6$-glucose tracing data, we compared the m + 3 to m + 2 ratios of TCA cycle derivatives as a proxy for PC vs. PDH activities. Elevated m + 3/m + 2 isotopologue ratios of aspartate, glutamate, and glutamine were observed in Ant2$^{-/-}$ T cells compared to WT, indicating a relative increase in PC contribution (Fig. 6P). Thirdly, we examined PDH phosphorylation at serine 300, an inhibitory modification, as an indirect indicator of PC activity[59,61]. Immunoblot analysis revealed an increase in phosphorylated PDH on serine 300 in naïve Ant2$^{-/-}$ CD8$^+$ T cells compared to WT cells (Fig. 6Q), suggesting increased pyruvate flow towards other available pathways, such as PPP, PC, and lactate dehydrogenase (LDH).

These findings indicate that Ant2$^{-/-}$ T cells adapt to reduced NAD$^+$/NADH and increased AMP/ATP ratios by upregulating anabolic pathways, including aerobic glycolysis, proline biosynthesis, creatine shuttle activity, nucleotide metabolism, and altered TCA cycle function. Interestingly, these metabolic changes resemble those seen in activated T cells, suggesting a reprogramming that supports anabolic metabolism required for effector function and proliferation.

Reduced NAD$^+$/NADH ratio-driven metabolic adaptations underlie enhanced proliferation in Ant2-deficient T cells

The metabolic adaptations observed in naïve Ant2-deficient T cells, including increased aerobic glycolysis and mitochondrial reprogramming, appear to correlate with the reduced NAD$^+$/NADH ratio resulting from Ant2 deficiency, potentially leading to the observed enhanced T cell proliferation. To investigate this link, we manipulated the NAD$^+$/NADH ratio using specific compounds.

Treatment with AZD7545[10], a pyruvate dehydrogenase kinase (PDK) inhibitor that decreases the NAD$^+$/NADH ratio, abrogated the superior proliferation of Ant2$^{-/-}$ CD8$^+$ T cells and matching their proliferation rates to WT cells at higher doses, demonstrating a direct dependence on NAD$^+$ regeneration via aerobic glycolysis (Fig. 7A, B). Conversely, increasing the NAD$^+$/NADH ratio using α-ketobutyrate (αKB)[62], significantly enhanced Ant2$^{-/-}$ CD8$^+$ T cell proliferation, while having a lesser impact on their WT counterparts, highlighting the critical role of NAD$^+$ replenishment in supporting their rapid growth (Fig. 7C-D). These results suggest that the inherent reliance of Ant2$^{-/-}$ T cells on aerobic glycolysis for redox balance, even in the naïve state, primes them for enhanced proliferation upon activation compared to WT T cells. Notably, this adaptation involves altered glucose utilization, rather than increased glucose dependency (Supplementary Fig. 7A–E) or uptake (Supplementary Fig. 7F–H).

To further dissect the contribution of mitochondrial reprogramming, including increased mitobiogenesis and mtROS production, we treated cells with SR-18292[63] (PGC1α inhibitor) and MitoQ[64] (mtROS scavenger). Both treatments resulted in decreased proliferation, with WT T cells exhibiting greater sensitivity (Fig. 7E–J). Specifically, SR-18292 treatment not only resulted in a more significant reduction in WT T cell proliferation, but also induced a greater level of apoptosis compared to Ant2$^{-/-}$ T cells (Supplementary Fig. 7I, J). These results suggest that the pre-existing mitochondrial adaptations in Ant2$^{-/-}$ T cells provide a proliferative advantage, with increased mitobiogenesis supporting initial growth and elevated mtROS enhancing activation propensity.

These findings strongly support our notion that mitochondrial reprogramming in Ant2$^{-/-}$ T cells at the naïve state provides them an advantage over their WT counterparts. This pre-activation reprogramming primes Ant2$^{-/-}$ T cells for superior proliferation, effectively bypassing the typical metabolic constraints faced by WT cells during activation.

Pharmacological inhibition of ANT augments naïve T cell activation and anti-tumor activity

The results of our study demonstrate that disrupting mtATP transfer to the cytosol and altering the redox state in naïve T cells, achieved

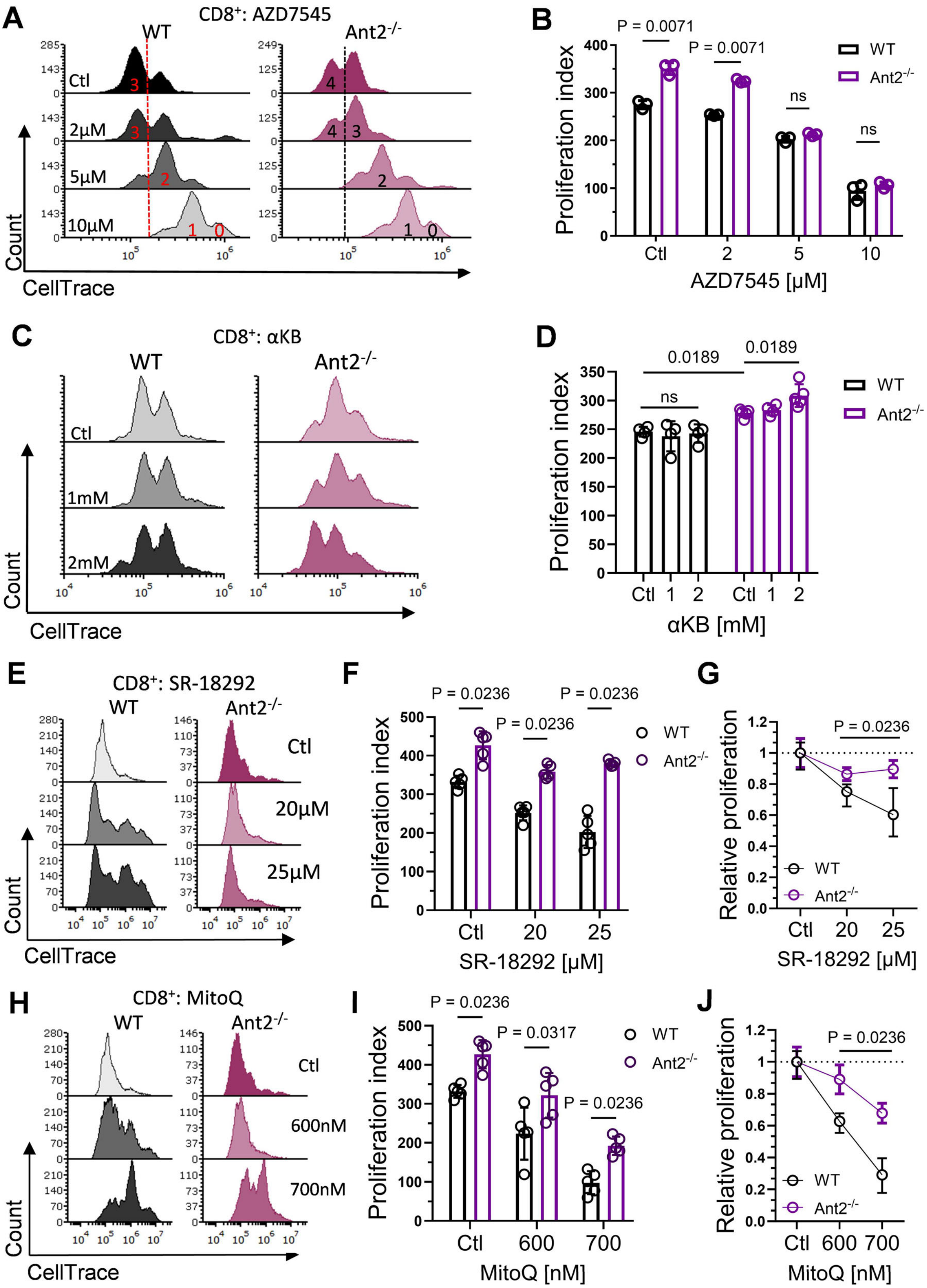

through Ant2 knockout, initiates metabolic rewiring that increases their propensity for activation. Therefore, we aimed to explore the therapeutic potential of these findings by using pharmacological pan-ANT inhibitors[65].

Previous studies have shown that prolonged ANT inhibition by atractyloside (ATR) and carboxyatractyloside (CATR) in vivo leads to metabolic rewiring, resulting in improved outcomes for the organism[16,66,67]. We investigated the effects of prolonged ANT inhibition using both inhibitors on T-cell function in vivo. To test T-cell activation, donor OT-I mice received daily injections of CATR (2.5 mg/kg) or PBS (control) for two weeks. The OT-I donor cells were labeled with CellTrace and then adoptively transferred intravenously into WT recipient mice. After 24 h, the recipient mice were injected intraperitoneally with OVA. Seventy-two hours after the OVA injection,

Fig. 7 | Reduced NAD$^+$/NADH ratio-driven metabolic adaptations and mitochondrial reprogramming underlie enhanced proliferation in Ant2-deficient T cells. **A** Representative flow cytometry histograms depict the CellTrace intensity of activated CD8$^+$ T cells derived from WT or Ant2$^{-/-}$ mice, treated with AZD7545 at the indicated concentrations. **B** Bar graph summarizing the results in A as a proliferation index (n = 3). **C** Same as (**A**) for cells treated with α-ketobutyrate at the indicated concentrations. **D** Bar graph summarizing the results in (**C**) as a proliferation index (WT: n = 4, Ant2$^{-/-}$: n = 5). **E** Same as A for cells treated with SR-18292 at the indicated concentrations. **F** Bar graph summarizing the results in (**E**) as a proliferation index (n = 5). **G** Graph showing the relative proliferation of WT or Ant2$^{-/-}$ CD8$^+$ T cells treated with the indicated concentrations of SR-18292. Relative proliferation was assessed by calculating the ratio of each treated sample's P. index to the average P. index of the corresponding untreated control (WT or Ant2$^{-/-}$). **H** Same as (**A**) for cells treated with MitoQ at the indicated concentrations. **I** Bar graph summarizing the results in (**H**) as a proliferation index (n = 5). **J** Same as G for cells treated with MitoQ. Statistical method: two-tailed Mann–Whitney test (**B**, **F**, **G**, **I**, **J**), or two-ways ANOVA (**D**). Data are represented as mean ± S.D. *n* refers to the number of biologically independent samples. ns = not significant. Source data are provided as a Source Data file.

CD8$^+$ T cells from the spleen of recipient mice were analyzed for CellTrace intensity and intracellular IFNγ staining after a brief ex vivo restimulation (Fig. 8A). As anticipated, ANT inhibition by CATR resulted in a significant increase in T cell proliferation (Fig. 8B, C) and IFNγ production (Fig. 8D, E).

Next, to assess the effect of ANT inhibition on T cell anti-tumor activity and mitobiogenesis, we used the well-established B16-OVA tumor-bearing mouse model. Donor OT-I/mtDendra2 mice were pretreated with either ATR (1 mg/kg) or PBS (control) for 10 days. Subsequently, T cells from the spleen of the donor mice were immediately analyzed for mtDendra2 intensity before being activated ex vivo with the SIINFEKEL peptide for 2 days. The activated T cells were then adoptively transferred into sublethally irradiated recipient mice bearing B16-OVA tumors. Tumor growth was monitored daily. Our findings demonstrate that ATR-treated naïve T cells significantly increased mitochondrial biomass (Fig. 8F), as indicated by mtDendra2 intensity. In addition, they also showed increased IFNγ production, with comparable granzyme b expression (Fig. 8G, H). Furthermore, both OT-I and ATR-treated OT-I T cells inhibited tumor growth compared to control mice that did not receive adoptive cell therapy (ACT), with ATR-treated OT-I T cells showing significantly greater tumor growth inhibition compared to untreated OT-I T cells (Fig. 8I–K). Overall, these findings strongly support our overarching concept: restricting mtATP transfer to the cytosol induces metabolic adaptations that enhance responsiveness to activation stimuli, which may be used for therapeutic purposes.

Discussion

The immune system's ability to respond effectively to threats requires a delicate balance between T-cell activation and regulation. Recent studies have unveiled the compelling role of metabolism in molding T-cell behavior, with metabolic reprogramming and checkpoints emerging as crucial determinants of T-cell fate and function[5,23,68]. Indeed, these cells exhibit remarkable adaptability even in challenging circumstances and hostile surroundings. While other cell types might falter, T cells demonstrate an exceptional ability to adjust through diverse metabolic pathways, shuttles, and "venting" strategies[10,69]. Here, we explore the intricate interplay between mitochondrial dynamics, bioenergetics, and immune function by investigating the effects of indirect OXPHOS restriction induced by Ant2 knockout.

Ant2 deletion has varied tissue-specific effects. It protects against non-alcoholic fatty liver disease (NAFLD) in the liver[16], improves glucose tolerance and insulin resistance in adipose tissue[70], and induces a proinflammatory phenotype in macrophages[71]. Most recently, it protects against obesity-induced renal dysfunction[67]. However, whole-body or cardiomyocyte-specific Ant2 knockout is lethal, emphasizing its critical role in these organs[14,72]. Here, we explore the intricate interplay between mitochondrial dynamics, bioenergetics, and immune function by investigating the effects of indirect OXPHOS restriction induced by Ant2 knockout. To surmount this metabolic bottleneck, both the cytosol and mitochondria of Ant2$^{-/-}$ T cells undergo significant metabolic adaptations. To maintain adequate NAD$^+$ levels in the face of OXPHOS restriction, naïve Ant2$^{-/-}$ T cells increase mitochondrial biogenesis and engage in mitochondrial reprogramming, concurrently enhancing aerobic glycolysis and proline biosynthesis. Additionally, the antioxidant defense mechanisms are upregulated to mitigate oxidative stress. Notably, mtROS levels remain slightly elevated, which may explain the heightened responsiveness to activation stimuli, consistent with previous studies identifying mtROS as crucial secondary messengers for T cell activation[73,74]. Further, we speculate that increased NADPH consumption by antioxidant activities and increased proline biosynthesis may prematurely induce glucose flux towards the PPP, potentially contributing to the observed nucleotide accumulation[75]. The summarized metabolic alterations are illustrated in Fig. 9.

Remarkably, many of these metabolic alterations observed in naïve Ant2-deficient T cells echo the metabolic rewiring characteristic of recently activated T cells, albeit driven by a distinct rationale[3,61]. In the context of activated T cells, the pursuit of biosynthetic precursors becomes paramount for enabling rapid proliferation[76]. This heightened biosynthetic demand prompts increased OXPHOS activity, aimed at sustaining a favorable NAD$^+$ to NADH ratio to support the oxidation reactions of the TCA cycle. OXPHOS upregulation gives rise to increased production of ROS, which further supports the activation signal[73]. This orchestrated response also alters glucose flux towards the PPP, facilitating the synthesis of nucleotides crucial for rapid cell proliferation. Nonetheless, it is well-established that the demand for NAD$^+$ outpaces that of ATP in rapidly proliferating cells[10], driving metabolic rewiring towards aerobic glycolysis and other alternative pathways for NAD$^+$ regeneration, such as proline biosynthesis. Hence, we propose that OXPHOS inhibition and its ensuing cascade of events in Ant2-deficient naïve T cells prompt an adaptive response akin to the metabolic programming witnessed in primed cells. As a substantial portion of their metabolic rewiring has already occurred, these naïve T cells appear to bypass the typical metabolic reprogramming associated with priming. Consequently, these naïve T cells manifest activated-like metabolic characteristics and behaviors.

Building on the metabolic adaptations observed in Ant2-deficient naïve T cells, our results demonstrate that prolonged pharmacological ANT inhibition, using ATR and CATR, recapitulates our Ant2$^{-/-}$ model in WT cells. Specifically, recipient mice receiving CATR-treated OT-I cells exhibited increased proliferation and IFNγ production upon restimulation, indicative of augmented activation. Similarly, in the B16-OVA tumor model, ATR-treated OT-I T cells demonstrated enhanced mitochondrial biomass, IFNγ production, and tumor growth inhibition compared to control T cells. The tumor microenvironment (TME) imposes significant functional burdens on effector T cells, particularly hypoxia, which necessitates metabolic adaptation. Hypoxia can lead to reduced OXPHOS, metabolic exhaustion, and functional impairment. Since naïve Ant2$^{-/-}$ T cells experience a chronic state of pseudohypoxia, characterized by elevated TMRM staining and restricted OXPHOS, they may exhibit enhanced resilience to the TME stressors. Therefore, "training" WT naïve T cells to mimic this pseudohypoxic state through prolonged ANT inhibition could potentially be a strategy to pre-condition their metabolism before encountering the TME. This approach holds promise for developing novel immunotherapies by leveraging ANT inhibitors to optimize T-cell function and efficacy

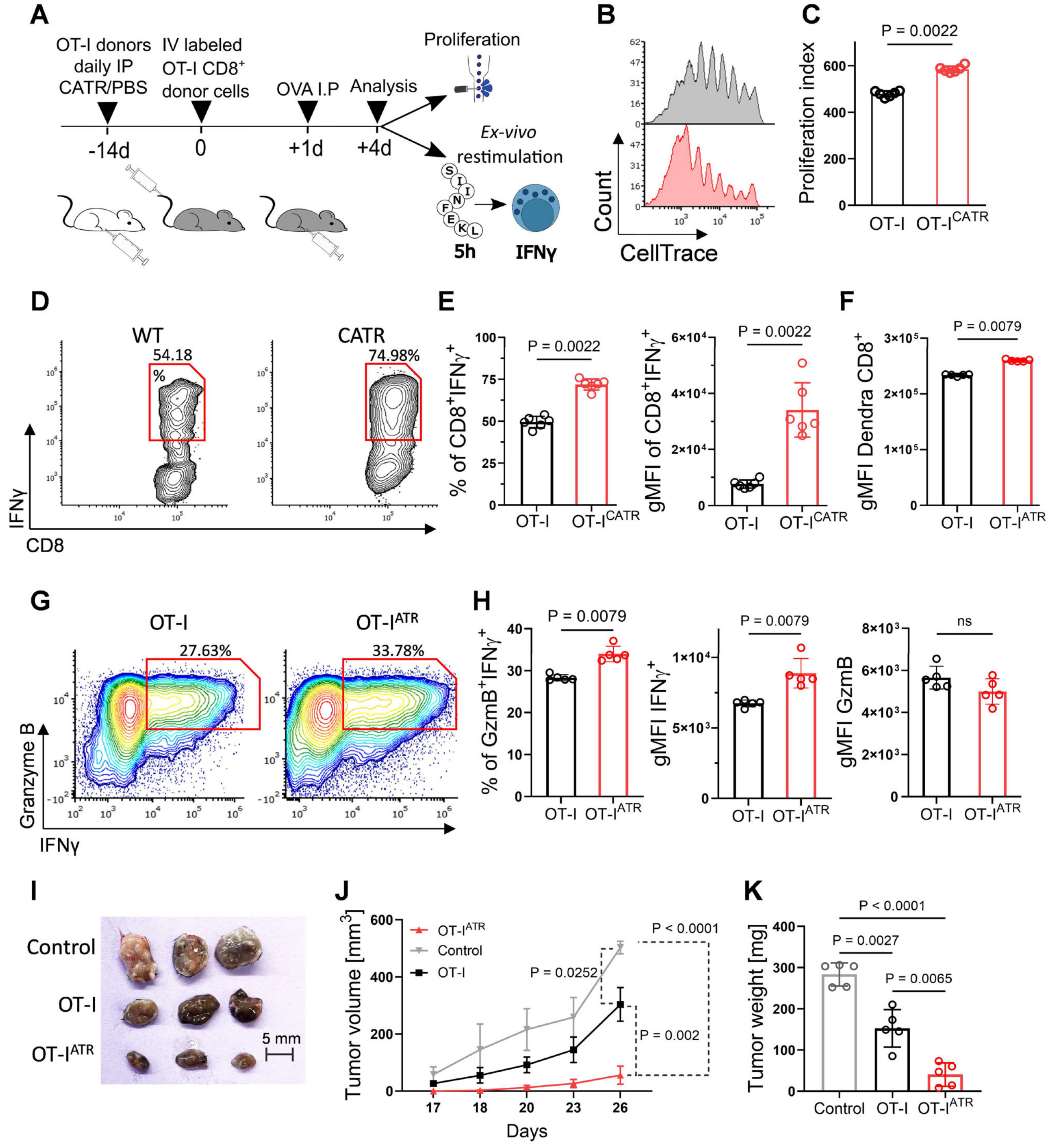

Fig. 8 | Pharmacological inhibition of ANT heightens naïve T cell responsiveness to activation stimuli. **A** Schematic of adoptive transfer: WT mice received daily i.p. injections of CATR or PBS for 14 days. Splenocytes were CellTrace-stained and transferred to WT recipients. Recipients received OVA i.p. one day post-transfer. Three days post-transfer, splenocytes were analyzed for CellTrace intensity and ex vivo restimulation with SIINFEKL peptide. **B** Representative flow cytometry histograms showing CellTrace intensity gated on donor PBS-treated (gray) or CATR-treated (red) WT OT-I T cells. **C** Graph depicting proliferation index of donor PBS-treated or CATR-treated WT OT-I T cells (n = 6). **D** Representative flow cytometry plots showing CD8 vs. IFNγ staining gated on donor PBS-treated (left) or CATR-treated (right) WT OT-I T cells. **E** Bar graphs summarizing the results shown in D as the frequency of $CD8^+IFN\gamma^+$ T cells (left), and gMFI of IFNγ gated on $CD8^+IFN\gamma^+$ T cells (right) (n = 6). **F–K** Female mice were injected subcutaneously with 1 × 106 B16-OVA tumor cells. Mice were then divided into three groups (n = 5 per group): control (no adoptive transfer), OT-I untreated, and ATR-treated OT-I $CD8^+$ T cell adoptive transfer groups. **F** Intensity of mtDendra2 in naïve OT-I $CD8^+$ T cells after spleen dissection. **G** Representative flow cytometry plots displaying IFNγ versus granzyme B (GzmB) staining in donor untreated and ATR-treated 24-h activated $CD8^+$ OT-I T cells. **H** Bar graphs summarizing the frequency of $IFN\gamma^+GzmB^+$ (left), and the gMFI of $IFN\gamma^+$ cells (middle), and gMFI of $GzmB^+$ cells (right), all gated on donor $CD8^+$ OT-I T cells. **I** Images of tumors from control, OT-I untreated, and ATR-treated OT-I $CD8^+$ T cell-injected mice at the end of the experiment (Scale bar: 5 mm). **J** Tumor volume (mm^3) was measured daily day 17 post-tumor implantation. **K** Tumors were excised, weighed, and presented as tumor weight (mg). Statistical method: two-tailed Mann–Whitney test (**C**, **E**, **F**, **H**), or two-way ANOVA test (**J**), or Kruskal–Wallis test (**K**). Data are represented as mean ± S.D for all expect ±SEM (**J**). *n* refers to the number of biologically independent samples. ns = not significant. Source data are provided as a Source Data file.

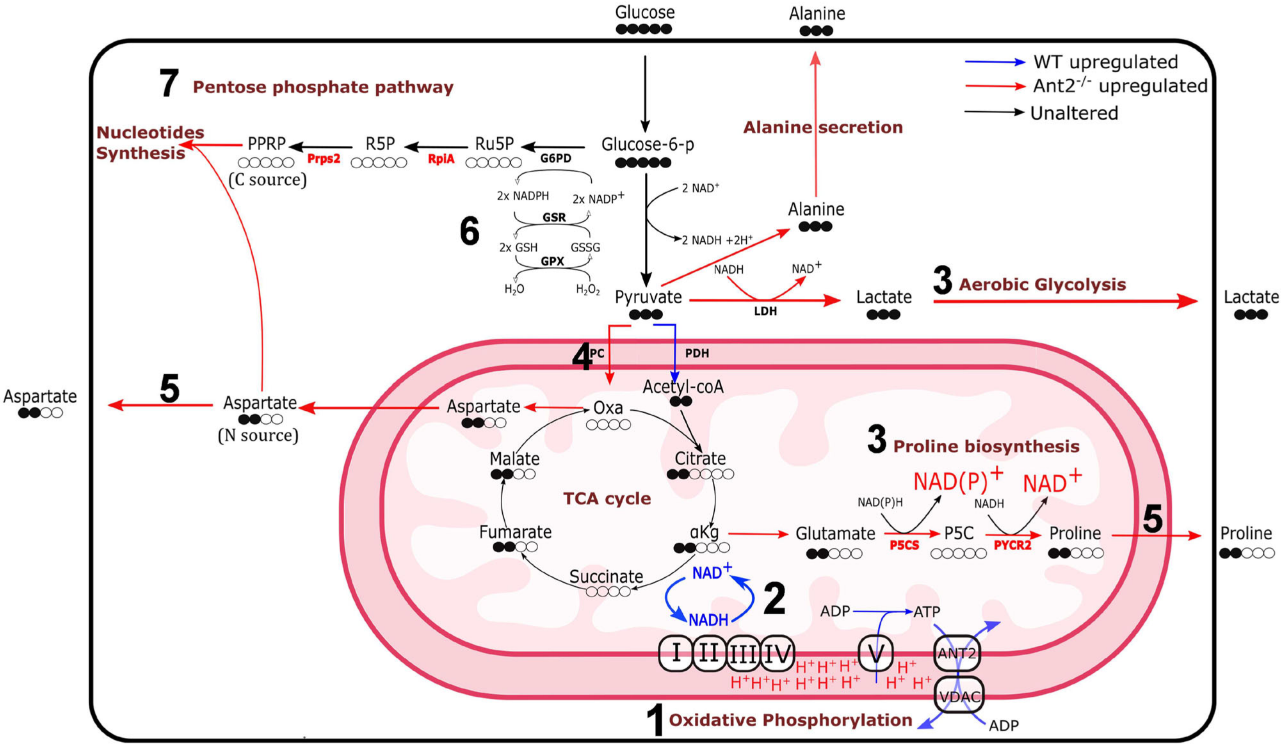

Fig. 9 | Metabolic alternations in Ant2$^{-/-}$ CD8$^+$ T cells. 1) Ant2 deficiency leads to a reduction in mtATP transfer to the cytosol, accompanied by a concomitant decrease in ADP concentrations within the mitochondrial matrix. 2) Functionality of the ATP-synthase complex is hindered, resulting in mitochondrial membrane hyperpolarization and OXPHOS inhibition. 3) Increased aerobic glycolysis and proline biosynthesis for NAD$^+$ regeneration. 4) Increased PC activity as a result of PDH inhibition. 5) Increased cataplerosis (TCA-cycle derived amino-acids). 6) Increased anti-oxidative stress machinery and NADPH consumption. 7) Increased phosphate pentose pathway activity due to increased NADPH consumption.

against tumors, or perhaps even infectious diseases, through targeted metabolic modulation.

Finally, our findings raise an intriguing question regarding the selective pressure for Ant2 function in T cells. Despite its plausible inhibitory effect on T cell activation, Ant2 is still selected to be expressed in T cells. Our results indicate that Ant2 deficiency prioritizes enhanced activation responses at the expense of homeostatic proliferation. Given that the balance between activation and homeostasis is crucial for immune system function, one can appreciate the potential role of Ant2 in upholding proper immunoregulation and averting overactivation and autoimmunity. Nonetheless, targeting Ant2 could hold beneficial effects in augmenting the effectiveness of therapeutic methods, like adoptive T cell transfer.

Methods

This study did not generate new, unique reagents.

Mice

The C57BL/6J (wild-type) mice (strain 000664), Slc25a5$^{tm1.1Nte}$/J mice (Ant2) (strain 029482), B6.Cg-Tg(dLck-cre)3779Nik/J mice (strain 012837), C57BL/6-Tg(TcraTcrb)1100Mjb/J (OT-I) mice (strain 00383), and B6.SJL-*Ptprc*^{a} *Pepc*^{b}/BoyJ mice (CD45.1) (strain 002014) were obtained from The Jackson Laboratory. B6;129S-Gt(ROSA)26Sor$^{tm1(CAG-COX8A/Dendra2)Dcc}$/J (mito-Dendra2) mice (The Jackson Laboratory, strain 018385) were a kind gift from Dr. Tsvee Lapidot from the Weizmann Institute of Science. Primer sequences are available at Supplementary table 1.

The T cell-specific Ant2 knockout mice were generated by crossing the mice above, containing a conditional floxed allele of Ant2 Slc25a5$^{tm1.1Nte}$/J (Ant2$^{flox/flox}$), with transgenic mice expressing Cre under the control of the distal Lck gene promoter (dLck-Cre). Once generated, mice were then crossed with OT-I mice to generate Ant2$^{-/-}$/OT-I mice, or crossed with mito-Dendra2 to generate Ant2$^{-/-}$/mito-Dendra2 mice, or triple crossed to generate Ant2$^{-/-}$/OT-I/mito-Dendra2 mice, per experimental design.

Control mice were littermates derived from the same breeding pairs as the Ant2 knockout mice and were generated using the same breeding strategy. Specifically, they were produced by crossing mice homozygous for the Ant2 floxed allele (Ant2^{2f}) with mice also homozygous for the Ant2 floxed allele but lacking the Cre recombinase gene. This strategy was used for all crosses, including those with OT-I and mito-Dendra2 mice, ensuring genetic consistency between experimental and control groups.

Mice were maintained and bred under specific-pathogen-free (SPF) conditions in the Hebrew University animal facilities according to Institutional Animal Care and Use Committee regulations. Mice were anesthetized with a combination of ketamine and xylazine, administered intraperitoneally. Following confirmation of deep anesthesia, as evidenced by the absence of a leg jerk reflex, cervical dislocation was performed.

Antibodies

A list of all antibodies is available at Supplementary table 2. The following antibodies were used for flow cytometry: anti-CD8α (53–6.7), anti-CD4 (GK1.5), Ki-67 (16A8), anti-CD3ε (145-2C11), anti-CD122 (5H4), anti-CD127 (A7R34), anti-CD62L (MEL-14), anti-CD44 (IM7), anti-CD69 (H1.2F3), anti-TCRβ (H57-597), anti-CD25 (PC61), anti-CD45.1 (A20), anti-CD45.2 (104), anti-TCR Vα2 (B20.1), and anti-IFNγ (XMG1.2). All antibodies were purchased from BioLegend.

For the activation of mouse T cells, purified anti-CD3ε (145–2C11) and anti-CD28 (37.51) antibodies obtained from BioLegend were employed at the appropriate concentrations as per the experiment design.

For immunoblotting, Antibodies to PDH phosphorylated on Ser^{300} (AP1064) and anti-PDH (ABS2082) were purchased from Sigma-Aldrich. The anti-Ant2 was acquired from Cell Signaling (14671). The anti-β-actin (sc-47778) and anti-β-tubulin (sc-5274) antibodies were purchased from Santa Cruz. These antibodies were diluted by 1:1000 in TBST, with 3% BSA and 0.05% sodium azide.

Validation of T cell-specific Ant2$^{-/-}$ mice by Polymerase Chain Reaction (PCR)

Total DNA extraction was performed on CD3^{+} cells that were isolated from WT or Ant2$^{-/-}$ mice using the "T cell isolation kit" (StemCell, 19851). Cells were then lysed in a "Tail Buffer" composed of 20 mM NaOH and 100 μM EDTA (BI, 01-862-1B). The mixture was incubated at 95 °C for 20 min. The PCR reaction was carried out by KAPA2G Fast ReadyMix (Sigma Aldrich, KK5103). Primers were designed targeting the intron 1 and intron 3 regions of the target DNA. The annealing temperature for the PCR was set to 65 °C for 34 cycles. Primer sequences are available at Supplementary Table 1.

cDNA preparation and Quantitative real-time PCR (qRT-PCR)

Total RNA was extracted from purified CD3^{+} cells that were isolated from WT or Ant2$^{-/-}$ mice using the "T cell isolation kit" (StemCell, 19851). Cells were then lysed using the Direct-zo RNA Mini Prep kit (Zymo Research). cDNA was synthesized from the isolated RNA using the ProtoScript First Strand cDNA Synthesis Kit (Bio-Labs). Quantitative real-time PCR using Applied Biosystems (AB), Viia 7 Real-Time PCR system with a Power SYBR green PCR master mix kit (Applied Biosystems, 4367660) according to the manufacturer's instructions. Primer sequences are available at Supplementary Table 1.

Mitochondrial DNA quantification

Total DNA (mitochondrial DNA and nuclear DNA) was extracted from CD8^{+} T cells that were isolated from WT or Ant2$^{-/-}$ mice using the "CD8^{+} T cell isolation kit" (StemCell, 19853). Cells were then lysed using the DNA extraction method (PCIA). Briefly, cell lysates were treated with lysis buffer composed of 10 mM Tris-HCl (pH 8), 1 mM EDTA, 0.5% SDS, and Proteinase K (80 units/ml) for overnight 55 °C incubation. The lysates were then centrifuged, and the supernatant was treated with PICA buffer (Sigma Aldrich, P2069). The upper layer containing DNA was then carefully transferred to another Eppendorf tube and mixed with an equal volume of chloroform. After homogenization, the samples were centrifuged again, and the upper layer was transferred to a new tube. 3 M NaAc was added (1:10), followed by an equivalent volume of cold (−20 °C) isopropanol. The mixture was incubated at −20 °C for 10 minutes and then centrifuged at 17,000 × *g* for 10 min. The supernatant was discarded, and the DNA pellet was washed with 1 ml of 70% ethanol. After centrifugation, the residual ethanol was removed, and the DNA pellet was dissolved in 40 μl of pre-heated (55 °C) double-distilled water (DDW). A concentration of 200 pg/ml of extracted DNA (total 800 pg/12 μl) was used in the RT-qPCR experiment.

Data was normalized to Mouse endogenous control (β2M) and analyzed using ΔΔCt model. Each experiment was performed in eight replicates and was repeated three times. Primer sequences are available at Supplementary table 1.

Immunoblotting

For anti-PDH immunoblot analysis, CD8^{+} T cells obtained from both WT and Ant2$^{-/-}$ mice were isolated using a "CD8^{+} T cell isolation kit" (StemCell, 19853). Alternatively, CD3^{+} cells were isolated using a "T cell isolation kit" (StemCell, 19851) for anti-Ant2 immunoblot. Subsequently, the isolated cells were lysed in RIPA buffer (Thermo Fisher Scientific, 89900) supplemented with protease and phosphatase inhibitors (Thermo Fisher Scientific, 78440). The quantification of protein content was conducted using the Bradford assay (Bio-Rad, 5000001). A total of 30 μg of protein was subjected to separation by SDS-PAGE and transferred to nitrocellulose membranes. Membranes were blocked with 5% BSA in TBST for 1 h at room temperature. After blocking, membranes were washed three times with TBST and incubated with primary antibodies overnight at 4 °C. After washing, membranes were incubated with horseradish peroxidase-conjugated secondary antibodies (Abcam, Ab98799 or 97085) for 30 min.

Flow cytometry

Spleens, thymus, and lymph nodes were harvested from mice and processed into single-cell suspensions using a 40 μm cell strainer (Fisher Scientific, 08-771-1) with either PBS, FACS buffer (PBS supplemented with 2% FBS and 1 mM EDTA), or FACS buffer without EDTA, as specified in the respective experimental design. Red blood cell lysis (Gibco, A10492-01) was performed according to the manufacturer's instructions. Cells were then washed, counted using a Denovoix CellDrop BF *brightfield cell counter*, and stained for cell-surface markers using various conjugated monoclonal antibodies (mAbs) in FACS buffer for 30 min at 4 °C.

For the staining of mitochondrial membrane potential, cells were treated with TMRM (Thermo Fischer, M20036) at a concentration of 50 nM in FACS buffer without EDTA for 30 min at 37 °C. Following this, the samples were maintained on ice for surface staining until they were ready for analysis. For more details on TMRM see Supplementary Table 2.

For intracellular staining, cells were fixed in 1% paraformaldehyde (PFA) in PBS for 15 min at RT. Cells were then washed with PBS, and permeabilized using a solution containing 0.1% saponin and intracellular mAbs in cold FACS buffer for 30 min. Stained cells were analyzed by a CytoFLEX Flow Cytometer with data being captured and processed using the CytExpert Software (Beckman Coulter, Inc).

Flow cytometry data were analyzed using the following gating strategy: cells were first gated on forward scatter area (FSC-A) vs. side scatter area (SSC-A) (Supplementary Fig. 8A) to select for single cells and exclude debris. A second gate was applied on side scatter area (SSC-A) vs. side scatter height (SSC-H) to further exclude doublets and cell aggregates (Supplementary Fig. 8B). Cells were then gated based on "positive" vs "negative" staining for specific markers, as calibrated in our laboratory (Supplementary Fig. 8C-S). The specific markers used for positive and negative gating are detailed in the respective Figure Legends. Subsequent analysis of the collected data was performed using FACS Express 6 software (De Novo Software).

Cell-cycle analysis

Splenocytes from WT and Ant2$^{-/-}$ mice were stained with surface markers for flow cytometry using the indicated antibodies in FACS buffer on ice for 20 min. Cells were then washed with PBS, fixed, and permeabilized by incubation in 1 mL of cold 70% ethanol at −20 °C for 1 h. Following fixation and permeabilization, cells were washed with cold PBS and stained with Ki-67 for 30 min on ice. After the Ki-67 staining, cells were washed in PBS, stained with DAPI in PBS, and immediately analyzed using a CytoFLEX flow cytometer.

Apoptosis detection

For apoptosis detection, splenocytes from WT and Ant2$^{-/-}$ mice were stained with Annexin V-FITC Apoptosis Staining/Detection Kit (abcam, ab14085) according to the manufacturer's instructions, including recommended concentrations and incubation times. Samples were immediately analyzed using a CytoFLEX flow cytometer.

In vivo T cell homeostatic expansion assay

CD45.1$^{+/+}$ WT recipient mice were sub-lethally irradiated (600 rad). One day following irradiation, an intravenous co-adoptive transfer was conducted (n = 4/group). This involved injecting 4×10^6 T cells in 200 μL in a 1:1 ratio of CD45.2$^{+/+}$ CFSE-labeled WT and CellTrace

(Thermo Fischer Scientific, M20036) labeled-Ant2$^{-/-}$-derived T cells, into the sub-lethally irradiated recipient mice. Reciprocal labeling was also performed. After 7 days, the mice were euthanized, and their splenocytes were isolated and examined by flow cytometry for CFSE and CellTrace intensities gated on naïve (CD44^{-}CD62L^{hi}) CD4^{+} and CD8^{+} donor T cells.

In vivo immunization assay for testing CD4^{+} T cell-mediated immunity

WT and Ant2$^{-/-}$ mice were subcutaneously immunized three times at 7-day intervals (n = 9/group). The first two immunizations included 100 μg/100 μl OVA protein (Sigma Aldrich, 9006-59-1) in complete Freund's adjuvant (CFA) (Sigma Aldrich, F5881), while the third immunization included OVA protein without CFA. After 21 days from the first vaccination, sera were collected and tested for OVA-specific IgG1 (Biolegend, 1144-05) and IgG2 (Biolegend, 1155-05) antibodies, as well as for the IFNγ (Biolegend, BLG-430804) and IL-4 (Biolegend, BLG-431104) cytokines using enzyme-linked immunosorbent assay (ELISA).

In vivo CD8^{+} T cell activation assay using Lenti-OVA

WT or Ant2$^{-/-}$ mice were primed intradermally in the ear pinna with 5×10^{6} transfection units (TU) of Lenti-OVA-GFP (A gift from Dr. Avihai Hovav from the Hebrew University of Jerusalem). Seven days after the viral challenge, mice were euthanized with ketamine and xylazine diluted in PBS, and their left and right cervical lymph nodes were dissected and analyzed by a flow cytometer.

In vivo T cell activation assay

CD45.1$^{+/+}$ WT recipient mice were intravenously (i.v.) administered CellTrace-labeled CD45.2$^{+/+}$ 2×10^{6} CD8^{+} T cells in 200 μL derived from WT or Ant2$^{-/-}$ OT-1 mice. After one day, recipient mice were intraperitoneally (i.p) injected with 30 μg of OVA protein (Sigma Aldrich, 9006-59-1). On day three following cell transfer, mice were euthanized, and their splenocytes were isolated and examined by flow cytometry for CellTrace intensity.

In-vivo CATR

Littermate OT-I mice were administered either carboxyatractyloside (CATR, AvaChem Scientific, 33286-30-5) at a dose of 2 mg/kg IP or vehicle for a duration of 2 weeks. CD8^{+} T cells from the donor mice were labeled with Cell-Trace and subsequently intravenously administered to recipient WT mice. On the following day, the recipient mice were injected intraperitoneally with 100 μg of OVA (Sigma Aldrich, 9006-59-1) design. After 3 days, the mice were euthanized, and their spleens were analyzed using flow cytometry to assess CellTrace intensity and IFNγ production. For IFNγ production, 1 M/100 μl splenocytes (flat 96-well plate) derived from OT-1 mice treated with either CATR or vehicle were restimulated with 1 μg/ml OVA-peptide for 6 h and Brefeldin A (Biolegend, 420601) for 4 h prior to analysis.

In-vivo B16-OVA melanoma tumor model

Donor mtDendra2/OT-I mice received daily IP injections of either PBS (mock) or 1 mg/kg Atractyloside (ATR, Cayman Chemical, 102130-43-8) for 10 days. Concurrently, 6-week-old female CD45.2 C57BL/6J recipient mice (Envigo) were anesthetized with ketamine and xylazine diluted in PBS, shaved, and injected subcutaneously on the right flank with 1 × 106 B16-OVA tumor cells in 100 μL HBSS (n = 5/group). Six days post-tumor injection (pti), donor mice were euthanized, and their T cells were activated in vitro with 0.5 μg/mL SIINFEKL peptide. Twenty-four hours post-activation, Granzyme B and IFNγ intensities were analyzed via flow cytometry. Seven days pti, recipient mice were sub-lethally irradiated (550 rad). Eight days pti (48 h post in-vitro activation), activated donor OT-1 T cells were adoptively transferred to the recipient mice. Tumor volumes were measured every 2–3 days. Mice were euthanized before the tumors 1400 mm^{3} or at the study endpoint (day 26). According to the Hebrew University ethics committee guidelines, the maximal tumor size permitted is 1400 mm^{3}. We confirm that the maximal tumor size was not exceeded during the course of this study.

In-vitro T cell for proliferation and cytokines production assay

Splenocytes derived from both WT and Ant2$^{-/-}$ mice were labeled with CellTrace and incubated with appropriate amounts of suspended anti-CD3ε and half the amount of anti-CD28 antibodies, or with 500 ng/ml SIINFEKL peptide, as per the experiment design. The incubation was in RPMI (Sigma Aldrich, 11875093) containing 10% Fetal Bovine Serum (Gibco), 2 mM Glutamine (Satorius, 03-042-1B), 100 U/ml penicillin-streptomycin (Satorius, 03-031-1B), and 50 μM β-mercaptoethanol (Merck, 60-24-2).

For the proliferation assay, cells were incubated for 72 h before analysis, with or without the following compounds: AZD7545 (Cayman, 252017-04-2), α-ketobutyrate (Sigma Aldrich, KO875), SR-18292 (MedChemExpress, HY-101491), and MitoQ (MedChemExpress, HY-100116A). The proliferation index reflects the sum of the percentage of cells in each generation group multiplied by the number of divisions.

For the IFNγ assay, cells were activated for 24 h and treated with Brefeldin A (Biolegend, 420601) 3 h before analysis.

In-vitro T cell killing assay

CD8^{+} T cells were negatively selected using StemCell kit (19853) from WT and Ant2$^{-/-}$-derived OT-I mice. Cells were activated in a 24-well plate coated with 2ug/ml of αCD3 and αCD28 antibodies for 5 days. Following this activation, the cells were incubated with either B16 (control) or B16 melanoma cells expressing ovalbumin (B16-OVA) target cells, maintaining a 1:1 ratio. After 6 h, the cells underwent three PBS washes. The remaining cells were subjected to an MTT assay. The percentage of killing was determined using the formula:

Percent of killing = 100 – {[(O.D. in B16-OVA with T cells – O.D. blank well)/O.D. in B16-OVA without T cells] × 100}. The calculated killing percentages were normalized to the control. Statistical analysis was conducted using the non-parametric Mann–Whitney test. The results are presented as mean ± SD, with *P* values indicated as *<0.01 and **<0.001.

Seahorse assay

Extracellular flux experiments were performed using a Seahorse XFe96 Extracellular Flux Analyzer (Seahorse Bioscience). CD8^{+} T cells were negatively selected using StemCellkit (19853) from WT and Ant2$^{-/-}$-derived OT-I mice. Naïve or activated CD8^{+} T cells (4×10^{5} or 2×10^{5} cells per well, respectively) were seeded in Seahorse XF 96 designated plates using 100 μg/ml poly-D-lysine (Sigma-Aldrich, A-003-E) and assayed according to the manufacturer's instructions. Briefly, RPMI 1640 medium (Bio-Rad, 11-100-1 K, without sodium bicarbonate) was supplemented with 2 mM glutamine (Satorius, 03-042-1B), 1 mM sodium pyruvate (Satorius, 03-022-1B), and 100 U/ml penicillin-streptomycin (Satorius, 03-031-1B). The following compound concentrations were used for the OCR measurements: 2 μM Oligomycin (Cayman Chemicals, 11342), 2 μM FCCP (Cayman Chemicals, 15218), and 1 μM Antimycin-A (Cayman Chemicals, 19433) and Rotenone (Cayman Chemicals, 13995). A total of 4 measurements per compound.

MitoSOX staining

WT and Ant2$^{-/-}$ splenocytes were incubated with pre-heated 1.5 μM MitoSOX red (Thermo Fisher Scientific, M36008) at 37 °C for 20 min. For control cells, a subset was pre-treated with 200 μM NAC (negative control) or 1 μM Antimycin A (positive control) in the incubator at 37 °C for 10 min using Eppendorf tubes. Subsequently, cells were washed with pre-warmed (37 °C) HBSS (from the same kit, ab228567) and immediately stained for MitoSOX along with the rest of the samples in a 96U well plate. After incubation, cells were washed twice in pre-warmed (37 °C) HBSS and then subjected to surface staining with FACS buffer using the indicated antibodies. For more details on MitoSOX see Supplementary Table 2.

Confocal microscopy

$CD8^+$ T cells were negatively selected using StemCell kit (19853) from WT and $Ant2^{-/-}$-derived mice. Cells were then seeded in high-resolution chamber (1.5H, 170 ± 5 µm) (Ibidi, IBD-80807) in FACS buffer. Pictures were obtained using a Zeiss LSM 980 with Airyscan on a Zeiss Axio Observer 7 SP inverted microscope using a Plan-Apochromat 63×/1.4 Oil DIC objective. Analysis was performed using the NIS-Elements (Nikon).

Protein mass spectrometry

Analysis was performed at the Stein Family mass spectrometry center in the Silberman Institute of Life Sciences, Hebrew University of Jerusalem.

Naïve $CD8^+$ T cells were negatively selected using StemCell kit (19858) from both WT and $Ant2^{-/-}$-derived OT-I mice. Cell lysates were sonicated in sonication bath for 15 min. Lysates were cleaned and digested using S-Trap microcolumns (Protifi, LLC, Huntington, NY) as specified by the manufacturer. In brief: DTT was added to samples to final concentration of 10 mM and incubated for 30 min at 37 °C. The proteins were alkylated in 55 mM iodoacetamide and incubated for 30 min at room temperature in the dark. Protein samples were acidified using phosphoric acid at a final concentration of 1.2%. Methanol-TRIS buffer (90% MeOH, 10% TRIS 0.5 M pH7.1) was added to the samples at a ratio of 6:1 (buffer: sample) and loaded onto S-Trap columns and subsequently washed twice with buffer. Sequencing grade modified trypsin (Promega Corp., Madison, WS) was loaded onto the column (1 µg per column) and incubated at 47 °C for 1 h. Peptides were eluted from column, acidified, and desalted on homemade C18 stage tips (Rappsilber J, Mann M, Ishihama Y. Protocol for micro-purification, enrichment, pre-fractionation and storage of peptides for proteomics using StageTips. Nat Protoc. 2007;2(8):1896-906.). A total of 0.75 µg of peptides (determined by Absorbance at 280 nm) from each sample were injected into the mass spectrometer.

MS analysis was performed using a Q Exactive-HF mass spectrometer (Thermo Fisher Scientific, Waltham, MA, USA) coupled on-line to an Ultimate 3000 Dionex (Thermo Fisher Scientific, Waltham, MA USA) UHPLC. Peptides were separated on a 120 min acetonitrile gradient run at a flow rate of 0.15 µl/min on a reverse phase 25-cm-long C18 column (75 µm ID, 2 µm, 100 Å, Thermo PepMapRSLC). Survey scans (300–1,650 m/z, target value 3E6 charges, maximum ion injection time 20 ms) were acquired and followed by higher energy collisional dissociation (HCD) based fragmentation (normalized collision energy 27). A resolution of 60,000 was used for survey scans and up to 15 dynamically chosen most abundant precursor ions, with "peptide preferable" profile were fragmented (isolation window 1.6 m/z). The MS/MS scans were acquired at a resolution of 15,000 (target value 1E5 charges, maximum ion injection times 25 ms). Dynamic exclusion was 20 sec. Data were acquired using Xcalibur software (Thermo Scientific). To avoid a carryover, the column was washed with 80% acetonitrile, 0.1% formic acid for 25 min between samples.

Mass spectra data were processed using the MaxQuant computational platform, version 1.6.6.0. Peak lists were searched against Mus musculus proteome obtained from Uniprot on 18.12.2019. The search included cysteine carbamidomethylation as a fixed modification, N-terminal acetylation and oxidation of methionine as variable modifications and allowed up to two miscleavages. The "match-between-runs" option was used. Peptides with a length of at least seven amino acids were considered and the required FDR was set to 1% at the peptide and protein level. Relative protein quantification in MaxQuant was performed using the label-free quantification (LFQ) algorithm (Cox, J. et al. MaxLFQ allows accurate proteome-wide label-free quantification by delayed normalization and maximal peptide ratio extraction. *Mol. Cell. Proteomics* 13, 2513–2526 (2014). The mass spectrometry proteomics data have been deposited to the ProteomeXchange Consortium via the PRIDE partner repository with the dataset identifier PXD062646.

Metabolomics and isotope tracing analysis

Naïve $CD8^+$ T cells were negatively selected using StemCell kit (19858) from WT and $Ant2^{-/-}$-derived OT-I mice. The cells were incubated with either 11 mM $^{13}C_6$-Glucose or 2 mM $^{13}C_5$-Glutamine for 4 h. Media extract: 40 µl of culture medium was added to 40 µl of a cold extraction solution (−20 °C) composed of methanol, acetonitrile, and water (5:3:2). Cell extracts: Cells were rapidly washed three times with ice-cold PBS, after which intracellular metabolites were extracted with 100 µl of ice-cold extraction solution for 5 min at 4 °C and subjected to 3 freeze-thaw cycles.

Media and cell extracts were centrifuged (10 min at 17,000 × *g*, 4 °C) to remove insoluble material, and the supernatant was collected for LC-MS analysis. Metabolomics data were normalized to protein concentrations using Bradford assay.

Briefly, the supernatants from the media and cell extracts were analyzed using a Thermo Ultimate 3000 high-performance liquid chromatography (HPLC) system coupled to a Q-Exactive Orbitrap Mass Spectrometer (Thermo Fisher Scientific). The resolution was 35,000 at 200 mass/charge ratio (m/z), and the electrospray ionization (ESI) mode was used with polarity switching to enable both positive and negative ions across a mass range of 67–1000 m/z.

The HPLC setup consisted of a ZIC-pHILIC column (SeQuant; 150 mm × 2.1 mm, 5 µm; Merck), with a ZIC-pHILIC guard column (SeQuant; 20 mm × 2.1 mm). 5 µl of biological extracts were injected, and the compounds were separated with a mobile phase gradient of 15 min, starting at 20% aqueous (20 mM ammonium carbonate adjusted to pH 2 with 0.1% of 25% ammonium hydroxide) and 80% organic (acetonitrile) and terminated with 20% acetonitrile. The flow rate and column temperature were maintained at 0.2 ml/min and 45 °C, respectively, for a total run time of 27 min.

All metabolites were detected using mass accuracy below five parts per million (ppm). Thermo Xcalibur was used for data acquisition. TraceFinder 4.1 was used for analysis. Peak areas of metabolites were determined by using the exact mass of the singly charged ions. The retention time of metabolites was predetermined on the pHILIC column by analyzing an in-house mass spectrometry metabolite library that was built by running commercially available standards.

Data analysis and statistics

The statistical significance of differences was determined by the two-tailed Mann–Whitney U test, or two-tailed Wilcoxon matched-pairs signed rank test, or two-tailed ANOVA test, or Benjamini–Hochberg method, or Kruskal–Wallis test, as described per figure legend. Data points exceeding two standard deviations (SDs) from the mean were considered outliers and excluded to ensure the robustness of the statistical analysis. Biological replicates refer to independent experimental replicates sourced from different mice donors. Technical replicates refer to independent experimental replicates from the same biological source. Differences with a P value of less than 0.05 were considered statistically significant. GraphPad prism and Perseus programs were used. MS data was normalized by ranking. Missing values were imputed using a normal distribution to avoid zero bias. Sample sizes were chosen based on our previous experience with similar experiments and on sample sizes reported in previous publications in the field. Sample sizes were chosen to ensure sufficient statistical power to detect biologically meaningful differences between groups, while also minimizing the number of animals used in accordance with ethical guidelines. We aimed for a minimum of [$n = 3$] animals per group, which we deemed sufficient based on the expected effect size and variability observed in pilot experiments. All mice were maintained on the C57BL/6J background and used for experiments at 6–12 weeks of age. All experiments were performed at least three times independently with at least two biological replicates, unless otherwise stated. Each biological replicate consisted of at least five technical replicates ($n = 5$) per biological sample.

Sex was considered in the study design. Wild-type (WT) and Ant2$^{-/-}$ littermates were sex-matched within experimental groups (i.e., WT female vs. Ant2$^{-/-}$ female, WT male vs. Ant2$^{-/-}$ male). This approach ensured that comparisons were made between genotypes within the same sex, thereby controlling for potential sex-based differences in T cell responses. No direct comparisons between male and female mice were performed. For tumor-bearing experiments, only female mice were used as both recipients and donors. This design choice was made due to established protocols within our laboratory for this specific tumor model, which has historically utilized female recipients. Therefore, sex-based analyzes were not performed within these experiments.

Large Language Models (LLMs)

We acknowledge the use of LLMs, specifically ChatGPT and Gemini, in the preparation of this manuscript. These AI tools were used to assist with language and grammar editing, as well as to refine and improve the clarity of our existing sentences. We emphasize that the LLMs did not generate any "de-novo" sentences or results; they were solely used to enhance the presentation of our own original research and writing.

Animal welfare

All animals were housed in a pathogen-free facility of The Hebrew University of Jerusalem with access to food and water and maintained under controlled conditions of humidity, temperature, and light/dark cycles, in accordance with the guidelines and regulations of the Institutional Animal Care and Use Committee (IACUC). Animal health and welfare were monitored regularly by the veterinary staff of the Animal Facility. All animal experiments were conducted under approved protocol [OPRR-A01-5011]. All efforts were made to minimize animal suffering and reduce the number of animals used.

Reporting summary

Further information on research design is available in the Nature Portfolio Reporting Summary linked to this article.

Data availability

All data are included in the Supplementary Information or available from the authors, as are unique reagents used in this Article. The raw numbers for charts and graphs are available in the Source Data file whenever possible. The mass spectrometry proteomics data have been deposited in the PRIDE database under the accession number PXD062646 [https://www.ebi.ac.uk/pride/archive/projects/PXD062646]. The dataset is publicly available at https://www.ebi.ac.uk/pride/archive/. The metabolomics data have been deposited into the MassIVE repository under the accession number MSV000097585 and can be accessed via the https://doi.org/10.25345/C5V40KB5K. The dataset is publicly available at https://massive.ucsd.edu. Other data and information is available on request. Data requests can be made to the principal investigator Prof. Michael Berger at: michaelb@ekmd.huji.ac.il OR to Dr. Omri Yosef at: omri.yoseph@gmail.com Source data are provided with this paper.

References

1. Reina-Campos, M., Scharping, N. E. & Goldrath, A. W. CD8+ T cell metabolism in infection and cancer. *Nat. Rev. Immunol.* **21**, 718–738 (2021).
2. Pearce, E. L., Poffenberger, M. C., Chang, C.-H. & Jones, R. G. Fueling immunity: insights into metabolism and lymphocyte function. Science **342**. https://doi.org/10.1126/science.1242454 (2013).
3. Chapman, N. M., Boothby, M. R. & Chi, H. Metabolic coordination of T cell quiescence and activation. *Nat. Rev. Immunol.* **20**, 55–70 (2020).
4. Bantug, G. R., Galluzzi, L., Kroemer, G. & Hess, C. The spectrum of T cell metabolism in health and disease. *Nat. Rev. Immunol.* **18**, 19–34 (2018).
5. Wang, R. & Green, D. R. Metabolic checkpoints in activated T cells. *Nat. Immunol.* **13**, 907–915 (2012).
6. Klein Geltink, R. I., Kyle, R. L. & Pearce, E. L. Unraveling the complex interplay between T cell metabolism and function. https://doi.org/10.1146/annurev-immunol (2018).
7. McBride, H. M., Neuspiel, M. & Wasiak, S. Mitochondria: more than just a powerhouse. *Curr. Biol.* **16**, R551–R560 (2006).
8. Martínez-Reyes, I. et al. TCA cycle and mitochondrial membrane potential are necessary for diverse biological functions. *Mol. Cell* **61**, 199–209 (2016).
9. Ron-Harel, N. et al. Mitochondrial biogenesis and proteome remodeling promote one-carbon metabolism for T cell activation. *Cell Metab.* **24**, 104–117 (2016).
10. Luengo, A. et al. Increased demand for NAD+ relative to ATP drives aerobic glycolysis. *Mol. Cell* **81**, 691 (2021).
11. Saragovi, A. et al. Systemic hypoxia inhibits T cell response by limiting mitobiogenesis via matrix substrate-level phosphorylation arrest. *Elife* **9**, 1–50 (2020).
12. Gropper, Y. et al. Culturing CTLs under hypoxic conditions enhances their cytolysis and improves their anti-tumor function. *Cell Rep.* **20**, 2547–2555 (2017).
13. Veliça, P. et al. Modified hypoxia-inducible factor expression in CD8+ T cells increases antitumor efficacy. *Cancer Immunol. Res* **9**, 401–414 (2021).
14. Cho, J. et al. Mitochondrial ATP transporter Ant2 depletion impairs erythropoiesis and B lymphopoiesis. *Cell Death Differ.* **22**, 1437–1450 (2015).
15. Kunji, E. R. S. et al. The transport mechanism of the mitochondrial ADP/ATP carrier. *Biochim. Biophys. Acta Mol. Cell Res.* **1863**, 2379–2393 (2016).
16. Cho, J. et al. Mitochondrial ATP transporter depletion protects mice against liver steatosis and insulin resistance. *Nat. Commun.* **8**, 14477 (2017).
17. Shah, D. K. "T-cell development in the thymus." Br Soc. Immunol. 1–2 (2014).
18. Bronstein-Sitton, N. et al. Sustained exposure to bacterial antigen induces interferon-γ-dependent T cell receptor ζ down-regulation and impaired T cell function. *Nat. Immunol.* **4**, 957–964 (2003).
19. Furmanov, K. et al. Diminished memory T-cell expansion due to delayed kinetics of antigen expression by lentivectors. *PLoS ONE* **8**, e66488 (2013).
20. Clarke, S. Rm. K. et al. Characterization of the ovalbumin-specific TCR transgenic line OT-I: MHC elements for positive and negative selection. *Immunol. Cell Biol.* **78**, 110–117 (2000).
21. Budhu, S. et al. CD8+ T cell concentration determines their efficiency in killing cognate antigen–expressing syngeneic mammalian cells in vitro and in mouse tissues. *J. Exp. Med.* **207**, 223–235 (2010).
22. Desdín-Micó, G., Soto-Heredero, G. & Mittelbrunn, M. Mitochondrial activity in T cells. *Mitochondrion.* **41**, 51–57 (2018).
23. Martínez-Reyes, I. & Chandel, N. S. Mitochondrial TCA cycle metabolites control physiology and disease. https://doi.org/10.1038/s41467-019-13668-3 (2020).
24. Chevrollier, A., Loiseau, D., Reynier, P. & Stepien, G. Adenine nucleotide translocase 2 is a key mitochondrial protein in cancer metabolism. *Biochim. Et Biophys. Acta Bioenerg.* **1807**, 562–567 (2011).
25. Stevens, J. F., Revel, J. S. & Maier, C. S. Mitochondria-centric review of polyphenol bioactivity in cancer models. *Antioxid. Redox Signal.* **29**, 1589–1611 (2018).

26. Pham, A. H., Mccaffery, J. M. & Chan, D. C. Mouse lines with photo-activatable mitochondria to study mitochondrial dynamics. *Genesis* **50**, 833–843 (2012).
27. Zhang, D. J. et al. Selective expression of the cre recombinase in late-stage thymocytes using the distal promoter of the *Lck* gene. *J. Immunol.* **174**, 6725–6731 (2005).
28. van der Windt, G. J. W., Chang, C. H. & Pearce, E. L. Measuring bioenergetics in T cells using a seahorse extracellular flux analyzer. *Curr. Protoc. Immunol.* 3.16B.1-3.16B.14. https://doi.org/10.1002/0471142735.im0316bs113 (2016).
29. van der Windt, G. J. W. et al. Mitochondrial respiratory capacity is a critical regulator of CD8 + T cell memory development. *Immunity* **36**, 68–78 (2012).
30. Nolfi-Donegan, D., Braganza, A. & Shiva, S. Mitochondrial electron transport chain: oxidative phosphorylation, oxidant production, and methods of measurement. *Redox Biol.* **37**, 101674 (2020).
31. Ahmad, T. et al. Computational classification of mitochondrial shapes reflects stress and redox state. *Cell Death Dis.* **4**, e461–e461 (2013).
32. Hung, C. H.-L. et al. A reciprocal relationship between reactive oxygen species and mitochondrial dynamics in neurodegeneration. *Redox Biol.* **14**, 7–19 (2018).
33. Calvo, S. E., Clauser, K. R. & Mootha, V. K. MitoCarta2.0: an updated inventory of mammalian mitochondrial proteins. *Nucleic Acids Res.* **44**, D1251–D1257 (2016).
34. Picca, A. & Lezza, A. M. S. Regulation of mitochondrial biogenesis through TFAM–mitochondrial DNA interactions: useful insights from aging and calorie restriction studies. *Mitochondrion.* **25**, 67–75 (2015).
35. Lin, S. et al. The mitochondrial deoxyguanosine kinase is required for cancer cell stemness in lung adenocarcinoma. *EMBO Mol. Med.* 11. https://doi.org/10.15252/emmm.201910849 (2019).
36. Inigo, M., Deja, S. & Burgess, S. C. Annual review of nutrition, ins and outs of the TCA Cycle: the central role of anaplerosis. https://doi.org/10.1146/annurev-nutr-120420 (2021).
37. Mak, T. W. et al. Glutathione primes T cell metabolism for inflammation. *Immunity* **46**, 675–689 (2017).
38. Harris, I. S. et al. Glutathione and thioredoxin antioxidant pathways synergize to drive cancer initiation and progression. *Cancer Cell* **27**, 211–222 (2015).
39. Ma, E. H. et al. Serine is an essential metabolite for effector T cell expansion. *Cell Metab.* **25**, 345–357 (2017).
40. Ron-Harel, N. et al. Defective respiration and one-carbon metabolism contribute to impaired naïve T cell activation in aged mice. *Proc. Natl. Acad. Sci. USA* **115**, 13347–13352 (2018).
41. Dutt, S., Hamza, I. & Bartnikas, T. B. Molecular mechanisms of iron and heme metabolism. *Annu. Rev. Nutr.* **42**, 311–335 (2022).
42. Berg, V. et al. Iron deprivation in human T cells induces non-proliferating accessory helper cells. *Immunohorizons* **4**, 165–177 (2020).
43. Jennifer, B. et al. Transferrin receptor 1 is a cellular receptor for human heme-albumin. *Commun. Biol.* **3**, 621 (2020).
44. Teh, M. R., Frost, J. N., Armitage, A. E., & Drakesmith, H. Analysis of iron and iron-interacting protein dynamics during t-cell activation. *Front. Immunol.* **12**. https://doi.org/10.3389/fimmu.2021.714613 (2021).
45. Zhou, Y. et al. Metascape provides a biologist-oriented resource for the analysis of systems-level datasets. *Nat. Commun.* **10**. https://doi.org/10.1038/s41467-019-09234-6 (2019).
46. Samborska, B. et al. Creatine transport and creatine kinase activity is required for CD8+ T cell immunity. *Cell Rep.* **38**. https://doi.org/10.1016/j.celrep.2022.110446 (2022).
47. Di Biase, S. et al. Creatine uptake regulates CD8 T cell antitumor immunity. *J. Exp. Med.* **216**, 2869–2882 (2019).
48. Greenhaff, P. L. The creatine-phosphocreatine system: there's more than one song in its repertoire. *J. Physiol.* **537**, 657–657 (2001).
49. Esterhuizen, K., van der Westhuizen, F. H. & Louw, R. Metabolomics of mitochondrial disease. *Mitochondrion* **35**, 97–110 (2017).
50. Schwörer, S. et al. Proline biosynthesis is a vent for TGFβ-induced mitochondrial redox stress. *EMBO J.* **39**. https://doi.org/10.15252/EMBJ.2019103334 (2020).
51. Phang, J. M. The proline regulatory axis and cancer. *Front. Oncol.* **0**, 60. https://doi.org/10.3389/FONC.2012.00060 (2012).
52. Phang, J. M. Proline metabolism in cell regulation and cancer biology: recent advances and hypotheses. https://doi.org/10.1089/ars.2017.7350 (2019).
53. Yang, Z. et al. Pyrroline-5-carboxylate synthase senses cellular stress and modulates metabolism by regulating mitochondrial respiration. *Cell Death Differ.* **28**, 303–319 (2020).
54. Westbrook, R. L. et al. Proline synthesis through PYCR1 is required to support cancer cell proliferation and survival in oxygen-limiting conditions. *Cell Rep.* **38**, 110320 (2022).
55. Phang, J. M. et al. Stimulation of the hexosemonophosphate-pentose pathway by pyrroline-5-carboxylate in cultured cells. *J. Cell Physiol.* **110**, 255–261 (1982).
56. Balmer, M. L. & Hess, C. Starving for survival—how catabolic metabolism fuels immune function. Curr. Opin. *Immunol.* **46**, 8–13 (2017).
57. Owen, O. E., Kalhan, S. C. & Hanson, R. W. The key role of anaplerosis and cataplerosis for citric acid cycle function *. *J. Biol. Chem.* **277**, 30409–30412 (2002).
58. Varanasi, S. K., Ma, S. & Kaech, S. M. T cell metabolism in a state of flux. *Immunity.* **51**, 783–785 (2019).
59. Elia, I. et al. Tumor cells dictate anti-tumor immune responses by altering pyruvate utilization and succinate signaling in CD8+ T cells. *Cell Metab.* **34**, 1137–1150.e6 (2022).
60. Kiesel, V. A. et al. Pyruvate carboxylase and cancer progression. *Cancer Metab.* 9. https://doi.org/10.1186/S40170-021-00256-7 (2021).
61. Menk, A. V. et al. Early TCR signaling induces rapid aerobic glycolysis enabling distinct acute T cell effector functions. *Cell Rep.* **22**, 1509–1521 (2018).
62. Sullivan, L. B. et al. Supporting aspartate biosynthesis is an essential function of respiration in proliferating cells. *Cell* **162**, 552–563 (2015).
63. Sharabi, K. et al. Selective chemical inhibition of PGC-1α gluconeogenic activity ameliorates type 2 diabetes. *Cell* **169**, 148–160.e15 (2017).
64. Rondeau, J. D. et al. Mitochondria-targeted antioxidant MitoQ radiosensitizes tumors by decreasing mitochondrial oxygen consumption. *Cell Death Discov.* **10**, 514 (2024).
65. Luciani, S., Martini, N. & Santi, R. Effects of carboxyatractyloside a structural analogue of atractyloside on mitochondrial oxidative phosphorylation. *Life Sci.* **10**, 961–968 (1971).
66. Zhang, P. et al. Atractyloside protect mice against liver steatosis by activation of autophagy via ANT-AMPK-mTORC1 signaling pathway. *Front. Pharmacol.* **12**. https://doi.org/10.3389/fphar.2021.736655 (2021).
67. Permyakova, A. et al. Renal mitochondrial ATP transporter ablation ameliorates obesity-induced CKD. *J. Am. Soc. Nephrol.* **35**, 281–298 (2024).
68. MacIver, N. J., Michalek, R. D. & Rathmell, J. C. Metabolic regulation of T lymphocytes. *Annu. Rev. Immunol.* **31**, 259–283 (2013).
69. Broeks, M. H. et al. The malate-aspartate shuttle is important for de novo serine biosynthesis ll The malate-aspartate shuttle is important for de novo serine biosynthesis. *Cell Rep.* **42**. https://doi.org/10.1016/j.celrep.2023.113043 (2023).
70. Seo, J. B. et al. Knockdown of ANT2 reduces adipocyte hypoxia and improves insulin resistance in obesity. *Nat. Metab.* **1**, 86–97 (2019).
71. Moon, J. S. et al. ANT2 drives proinflammatory macrophage activation in obesity. *JCI Insight* 6. https://doi.org/10.1172/jci.insight.147033 (2021).

72. Kokoszka, J. E. et al. Deficiency in the mouse mitochondrial adenine nucleotide translocator isoform 2 gene is associated with cardiac noncompaction. *Biochim. Et Biophys. Acta Bioenerg.* **1857**, 1203–1212 (2016).
73. Murphy, M. P. & Siegel, R. M. Mitochondrial ROS fire up T cell activation. *Immunity*. **38**, 201–202 (2013).
74. Sena, L. A. et al. Mitochondria are required for antigen-specific T cell activation through reactive oxygen species signaling. *Immunity* **38**, 225–236 (2013).
75. Ju, H.-Q. et al. NADPH homeostasis in cancer: functions, mechanisms and therapeutic implications. *Signal Transduct. Target. Ther.* **5**, 231 (2020).
76. Dimeloe, S., Burgener, A.-V., Grählert, J. & Hess, C. T-cell metabolism governing activation, proliferation and differentiation; a modular view. *Immunology*. **150**, 35–44 (2017).

Acknowledgements

This study was supported by grants from the Israel Science Foundation, No.2797/22 and No.883/22, Joint grant of the Hebrew University and Hadassah Medical Center, and the ICRF–CRI Immunotherapy Project Grant, a medical research grant from Israel Cancer Research Fund and Cancer Research Institute. We thank Tamar Burdo-Berger for creating the schematic illustrations used in this work.

Author contributions

O.Y.; Study Design, Data curation, Formal analysis, Investigation, Methodology, Writing—original draft, Project administration, Writing—review and editing. E.G. A.S. and M.H.; Insight Elaboration. I.A. and B.A. performed the metabolomics. L.C.D., O.S., W.S., V.L., and A.P. helped with experiments. Z.B.O., data analysis, and preformed the CD4$^+$ T-cell immunity experiment. J.T.; Resources. M.B.; Study Design, Supervision, Funding acquisition, Investigation, Methodology, Writing—original draft, Writing—review and editing.

Competing interests

The authors declare no competing interests.

Additional information

Supplementary information The online version contains supplementary material available at https://doi.org/10.1038/s41467-025-59310-3.

Correspondence and requests for materials should be addressed to Michael Berger.

Peer review information *Nature Communications* thanks the anonymous reviewer(s) for their contribution to the peer review of this work. A peer review file is available.

Reprints and permissions information is available at http://www.nature.com/reprints